nature

https://doi.org/10.1038/s41586-020-2673-2

Accelerated Article Preview

Structure of LRRK2 in Parkinson's disease and model for microtubule interaction

Received: 10 November 2019

Accepted: 12 August 2020

Accelerated Article Preview Published online 19 August 2020

Cite this article as: Deniston, C. K. et al. Structure of LRRK2 in Parkinson's disease and model for microtubule interaction. *Nature* https://doi.org/10.1038/s41586-020-2673-2 (2020).

C. K. Deniston, J. Salogiannis, S. Mathea, D. M. Snead, I. Lahiri, M. Matyszewski, O. Donosa, R. Watanabe, J. Böhning, A. K. Shiau, S. Knapp, E. Villa, S. L. Reck-Peterson & A. E. Leschziner

Structure of LRRK2 in Parkinson's disease and model for microtubule interaction

https://doi.org/10.1038/s41586-020-2673-2

Received: 10 November 2019

Accepted: 12 August 2020

Published online: 19 August 2020

C. K. Deniston[1,10], J. Salogiannis[1,2,10], S. Mathea[3,10], D. M. Snead[1], I. Lahiri[1,4], M. Matyszewski[1], O. Donosa[2], R. Watanabe[5,6], J. Böhning[5,7], A. K. Shiau[8,9], S. Knapp[3], E. Villa[5], S. L. Reck-Peterson[1,2,9]✉ & A. E. Leschziner[1,5]✉

Leucine-rich repeat kinase 2 (*LRRK2*) is the most commonly mutated gene in familial Parkinson's disease (PD)[1] and is also linked to its idiopathic form[2]. LRRK2 is proposed to function in membrane trafficking[3] and co-localizes with microtubules[4]. Despite LRRK2's fundamental importance for understanding and treating PD, there is limited structural information on it. Here we report the 3.5Å structure of the catalytic half of LRRK2, and an atomic model of microtubule-associated LRRK2 built using a reported 14Å cryo-electron tomography in situ structure[5]. We propose that the conformation of LRRK2's kinase domain regulates its microtubule interaction, with a closed conformation favouring oligomerization on microtubules. We show that the catalytic half of LRRK2 is sufficient for filament formation and blocks the motility of the microtubule-based motors kinesin-1 and cytoplasmic dynein-1 in vitro. Kinase inhibitors that stabilize an open conformation relieve this interference and reduce LRRK2 filament formation in cells, while those that stabilize a closed conformation do not. Our findings suggest that LRRK2 can act as a roadblock for microtubule-based motors and have implications for the design of therapeutic LRRK2 kinase inhibitors.

LRRK2 is a large (288 kDa) multi-domain protein. Its amino-terminal half is comprised of repetitive protein interaction motifs (Armadillo, Ankyrin, and Leucine-Rich Repeats) and its carboxy-terminal catalytic half contains a Ras-like GTPase (Ras-of-Complex, or RoC domain), a kinase domain, and two other domains (C-terminal Of Roc, or COR, and WD40) (Fig. 1a). High-resolution structural data on LRRK2 is limited to bacterial homologues[6,7] or isolated domains[8,9], whereas low resolution full-length protein structures have been obtained using negative stain[10] and cryo-electron microscopy (Cryo-EM)[11]. A recent study of LRRK2 bound to microtubules in cells using cryo-electron tomography (Cryo-ET) and subtomogram analysis led to a 14Å structure and proposed model of the catalytic half of LRRK2[5].

LRRK2's interaction with microtubules is linked to disease as four of the five major PD-causing mutations (Fig. 1a)[1] enhance microtubule association of LRRK2[12]. Further, Rab GTPases, which mark membranous cargos that move along microtubules, are physiological LRRK2 kinase substrates[13,14]. These cargos, and others implicated in PD pathology[3], are transported by the microtubule-based motors dynein and kinesin. Here, we set out to determine a high-resolution structure of LRRK2's catalytic half using cryo-EM, and to understand how it interacts with microtubules and how this impacts microtubule-based motor movement.

Structure of the catalytic half of LRRK2

High-resolution studies on human LRRK2 have been limited by the lack of efficient expression systems that yield stable protein. We tested many constructs (Extended Data Fig. 1a), leading to the identification of one consisting of the carboxy-terminal half of wild-type (WT) LRRK2 (amino acids 1,327 to 2,527), which resulted in robust insect cell expression and well-behaved protein (Extended Data Fig. 1b, c). This construct comprises the **R**oC, **C**OR, **k**inase and **W**D40 domains of LRRK2 (Fig. 1a), which we refer to as LRRK2^{RCKW}. The COR domain was previously defined as consisting of two subdomains, COR-A and COR-B[6].

We determined a 3.5Å structure of LRRK2^{RCKW} in the presence of GDP using cryo-EM (Fig. 1b, c and Extended Data Figs. 1 and 2). On our grids, we observed a mixture of monomers, dimers and head-to-tail trimers; we used the trimer to solve the structure (Fig. 1b and Extended Data Figs. 1 and 2). Although critical for reaching high resolution, the trimer is likely specific to the cryo-EM grid preparation as LRRK2^{RCKW} is predominantly monomeric, with a smaller percentage of dimers, in solution (Extended Data Fig. 2n) and we only observed the trimer when preparing grids with high concentrations of LRRK2^{RCKW} (see Methods). Due to flexibility, the RoC and COR-A domains were lower resolution in our structure (Fig. 1b, c). We improved this part of the map using signal subtraction and focused 3D classification and refinement (Fig. 1d, e, Extended Data Fig. 2a-d). The final model was generated using the signal subtracted maps of the RoC and COR-A domains, and then combined with the COR-B, kinase and WD40 domains from the trimer map (Fig. 1f, Extended Data Fig. 2e-m and Supplementary Video 1). Our model fits well into an 8.1Å reconstruction we obtained of a LRRK2^{RCKW} monomer (Fig. 1g, and see Extended Data Fig. 6), indicating that trimer formation does not cause major structural changes in the protein.

[1]Department of Cellular and Molecular Medicine, University of California San Diego, La Jolla, CA, USA. [2]Howard Hughes Medical Institute, Chevy Chase, MD, USA. [3]Institute of Pharmaceutical Chemistry, Goethe-Universität, Frankfurt, Germany. [4]Present address: Department of Biological Sciences, Indian Institute of Science Education and Research Mohali, Mohali, Punjab, India. [5]Division of Biological Sciences, Molecular Biology Section, University of California San Diego, La Jolla, CA, USA. [6]Present address: La Jolla Institute for Immunology, La Jolla, CA, USA. [7]Present address: Sir William Dunn School of Pathology, Oxford University, Oxford, UK. [8]Small Molecule Discovery Program, Ludwig Institute for Cancer Research, La Jolla, CA, USA. [9]Division of Biological Sciences, Cell and Developmental Biology Section, University of California San Diego, La Jolla, CA, USA. [10]These authors contributed equally: C. K. Deniston, J. Salogiannis, S. Mathea. ✉e-mail: sreckpeterson@ucsd.edu; aleschziner@ucsd.edu

LRRK2^{RCKW} adopts an overall J-shape, with the WD40, kinase and COR-B domains arranged along one axis, and COR-A and RoC turning around back towards the kinase. This brings the COR-A and tightly associated RoC domain into close proximity to the kinase's C-lobe (Fig. 1f, and Supplementary Video 1). This arrangement likely underpins the crosstalk between LRRK2's kinase and GTPase[15,16]. Part of the FERM domain in the FAK-FERM complex approaches the FAK C-lobe in a similar way[17] (Extended Data Fig. 3a, b). The RoC, COR-A and COR-B domains are arranged as seen in crystal structures of LRRK2 bacterial homologues[6,7,18]. The N-lobe of the kinase domain, in particular its αC helix, forms an extensive interaction with the COR-B domain, with COR-B occupying a location similar to Cyclin A in CDK2-Cyclin A[19] (Extended Data Fig. 3a, c).

The kinase in our LRRK2^{RCKW} structure is in an open, inactive conformation. Its activation loop contains the site of two familial PD mutations (G2019S and I2020T) and is disordered beyond G2019 (Fig. 1h, Extended Data Fig. 2h, and Supplementary Video 2). R1441 and Y1699 are the sites of three other familial PD mutations and are located at the RoC-COR-B interface (Fig. 1h, Extended Data Fig. 2j, and Supplementary Video 2). Given that the kinase and GTPase interact with each other via the COR-A domain, it is possible that these mutations, located at the interface between the GTPase and COR-B, alter the conformational landscape of LRRK2 in response to ligands and/or regulatory signals and thus affect the cross-talk between LRRK2's catalytic domains.

A unique feature of LRRK2 is a 28-amino acid α-helix located at its extreme C terminus, following the WD40 domain (Fig. 1i, j, and Supplementary Video 3). While a number of other kinases have α-helices in the same general location, none form interactions as extensive as those observed in LRRK2 (Fig. 1i, j, Extended Data Fig. 3d-i). Deletion of this helix resulted in an insoluble protein (Extended Data Fig. 1a, b). A residue near its end (T2524) is a known phosphorylation site for LRRK2[20]. Given the close proximity between T2524 and the N-lobe of the kinase domain, as well as the adjacent COR-B domain, we hypothesize that phosphorylation of this residue may play a role in regulating the kinase. Since the last two residues of the C-terminal helix are disordered in our structure, as is a neighbouring loop in COR-B, it is possible that conditions exist where these regions become ordered and turn the C-terminal helix into a scaffolding element that connects COR-B, the kinase and the WD40 domains.

We modelled the Leucine-Rich Repeats (LRR) into LRRK2^{RCKW} by using a crystal structure of the LRR, RoC, and COR domains of *C. tepidum*'s Roco protein[7] (Extended Data Fig. 3l-p). In our model, the LRR wraps around the N-lobe of the kinase and approaches the C-lobe, placing the known S1292 autophosphorylation site in the LRR close to the kinase's active site, and the Crohn's disease-associated residue N2081[21], located in the kinase's C-lobe, next to the LRR (Extended Data Fig. 3q), suggesting the functional relevance of this predicted interface.

Model of microtubule-bound filaments

Recently, a 14Å structure of microtubule-associated filaments of full-length LRRK2 (carrying the filament-promoting I2020T mutation[12]) was determined using in situ cryo-ET and subtomogram analysis[5] (Fig. 2a). The LRRK2 filaments formed on microtubules are right-handed[5]. Because microtubules are left-handed and no strong density connected the LRRK2 filament to the microtubule surface[5], it is unknown if LRRK2's microtubule interaction is direct. To address this, we combined purified microtubules and LRRK2^{RCKW}, either WT or I2020T, and imaged them by cryo-EM. Both WT and I2020T LRRK2^{RCKW} bound to microtubules, and diffraction patterns calculated from the images revealed layer lines consistent with the formation of ordered filaments (Fig. 2b). Thus, the interaction between LRRK2 and microtubules is direct and the catalytic C-terminal half of LRRK2 is sufficient for the formation of microtubule-associated filaments. The layer line patterns of WT and I2020T LRRK2^{RCKW} are different, with the I2020T diffraction pattern having an additional layer line of lower frequency, indicating longer-range order in the filaments (Fig. 2b). This is consistent with the observation that the I2020T mutation promotes microtubule association by LRRK2 in cells[12]. Understanding the structural basis for this effect will require high-resolution structures of the filaments formed by WT and I2020T LRRK2.

Previously, integrative modelling was used to build a model into the in situ structure of microtubule-associated LRRK2[5]. This modelling indicated that the well-resolved Cryo-ET density closest to the microtubule was comprised of the RoC, COR, Kinase and WD40 domains and gave orientation ensembles for each domain[5] that are in good agreement with our high-resolution structure of LRRK2^{RCKW} (Extended Data Fig. 4a). Here, we built an atomic model of the microtubule-bound LRRK2 filaments by combining our 3.5Å structure of LRRK2^{RCKW} with the 14Å in situ structure of microtubule-associated LRRK2 (Extended Data Fig. 4b-f). This revealed that the LRRK2^{RCKW} structure is sufficient to account for the density seen in the in situ structure (Fig. 2c), in agreement with our ability to reconstitute microtubule-associated LRRK2^{RCKW} filaments in vitro (Fig. 2b), and with the earlier modelling[5].

Although our LRRK2^{RCKW} structure fits the overall shape of the cryo-ET map, there were significant clashes at the COR domain interfaces (Fig. 2d). Since the kinase in our LRRK2^{RCKW} structure is in an open conformation, we hypothesized that filament formation might require LRRK2's kinase to be in a closed conformation. To test this, we modelled a kinase-closed LRRK2^{RCKW} (Fig. 2e and Extended Data Fig. 4g-j) and used it to rebuild the LRRK2 filament. The kinase-closed LRRK2^{RCKW} model resolved more than 80% of the backbone clashes we had observed with our kinase-open LRRK2^{RCKW} structure (Fig. 2c, d, f, g). A closed conformation for the kinase was also proposed by the integrative modelling[5]. Given this data, we hypothesize that the conformation of LRRK2 controls its ability to oligomerize on microtubules, with a closed kinase promoting oligomerization and an open (inactive) one disfavouring it (Fig. 2h, i).

The LRRK2 filaments in our kinase-closed model are formed by two homotypic interactions: one is mediated by the WD40 domain, and the other by the COR-A and COR-B domains (Fig. 3a–d). Similar interfaces were reported based on the cryo-ET structure[5]. We also solved structures of LRRK2^{RCKW} dimers, using the same grids that yielded the 3.5Å structure of LRRK2^{RCKW}. We obtained structures of both the WD40/WD40- and COR/COR-mediated dimers, indicating that both interfaces mediate dimerization in the absence of microtubules (Fig. 3e, f and Extended Data Figs. 5 and 6). The interface in the COR-mediated dimer of LRRK2^{RCKW} differs from that reported for the *C. tepidum* Roco protein[6,7]; while the GTPase domains interact directly in the dimer of the bacterial protein[7], they are not involved in the dimerization interface we observed for LRRK2 (Extended Data Fig. 6c).

We built an independent model of a closed-kinase LRRK2^{RCKW} by splitting our 3.5Å structure in half at the junction between the N- and C-lobes of the kinase, and fitting the fragments into our cryo-EM map of a WD40/WD40 dimer obtained in the presence of a LRRK2-specific Type I kinase inhibitor, MLi-2[22,23], which is predicted to stabilize the kinase closed conformation (Extended Data Fig. 7a-c). We then docked this closed-kinase model (Extended Data Fig. 7c) into the cryo-EM maps of WD40- and COR-mediated dimers obtained in the presence of MLi-2 to generate molecular models of both dimers (Extended Data Fig. 7d, e). We aligned these models to build a polymer *in silico*. This resulted in a right-handed helix with the same general geometric properties seen in the cellular LRRK2 filaments, indicating that those properties are largely encoded in the structure of LRRK2^{RCKW} itself (Fig. 3g, h, and Extended Data Fig. 7f). Docking the same two halves of LRRK2^{RCKW} into the cryo-EM map of a monomer we obtained in the absence of inhibitors or ATP led to a structure similar to our 3.5Å structure obtained from trimers, further confirming that trimer formation does not alter the conformation of LRRK2^{RCKW} (Extended Data Fig. 7g, h).

These data, along with the apparent lack of any residue-specific interactions between LRRK2 and the microtubule lattice, suggest that the microtubule may provide a surface for LRRK2 to oligomerize on using interfaces that exist in solution, thus explaining the symmetry mismatch between the microtubule and the LRRK2 filament. Consistent with this, the surface charge of the microtubule facing the LRRK2^{RCKW} filament is acidic, while there are basic patches on the LRRK2^{RCKW} filament facing the microtubule (Extended Data Fig. 7i-l). The unstructured C-terminal tails of α- and β-tubulin, which were not included in the surface charge calculations, are also acidic.

LRRK2^{RCKW} inhibits kinesin and dynein

To test our hypothesis that the conformation of LRRK2's kinase domain regulates its interaction with microtubules, we needed a sensitive assay to measure the association of LRRK2^{RCKW} with microtubules and a means to control the conformation of its kinase. We monitored microtubule association by measuring the effect of LRRK2^{RCKW} on microtubule-based motor motility. We used a truncated human kinesin-1, Kif5B ("kinesin")[24], which moves towards the microtubule plus end, and the activated human cytoplasmic dynein-1/ dynactin/ ninein-like complex ("dynein")[25], which moves in the opposite direction. Using single-molecule in vitro motility assays (Fig. 4a), we found that low nanomolar concentrations of LRRK2^{RCKW} inhibited both kinesin and dynein movement, with near complete inhibition at 25 nM LRRK2^{RCKW} (Fig. 4b, c and Extended Data Fig. 8a, b). We hypothesized that LRRK2^{RCKW} was acting as a roadblock for the motors. In agreement with this, the distance that single kinesins moved (run length) was reduced (Fig. 4d), while their velocity remained relatively constant (Fig. 4e). We obtained similar results with dynein (Fig. 4f). Other microtubule-associated proteins, such as MAP2 and Tau, also inhibit kinesin, but not dynein[26,27], likely due to dynein's ability to sidestep on the microtubule[28–30]. LRRK2's unusual ability to inhibit dynein may be a consequence of it forming oligomers that cannot be overcome by sidestepping.

We also tested the inhibition of kinesin by I2020T LRRK2^{RCKW}, which promotes filament formation when overexpressed in cells[12]. I2020T LRRK2^{RCKW} inhibited kinesin to a similar extent as WT LRRK2^{RCKW} (Extended Data Fig. 8c, d). Given that in vitro reconstituted filaments of I2020T LRRK2^{RCKW} show longer range order compared with WT LRRK2^{RCKW} (Fig. 2b), it is possible that the high sensitivity of the single-molecule motility assays does not allow us to distinguish differences in oligomer length and/or stability between WT and I2020T LRRK2^{RCKW}.

Type II inhibitors rescue the motors

Our hypothesis predicts that the closed conformation of LRRK2's kinase domain will favour LRRK2's oligomerization on microtubules. Conversely, it predicts that conditions that stabilize the kinase in an open conformation will prevent oligomerization and thus decrease microtubule binding by LRRK2^{RCKW}, resulting in relief of LRRK2^{RCKW}-dependent inhibition of kinesin and dynein motility. To test these predictions, we searched for a Type II kinase inhibitor that binds tightly to LRRK2 with structural evidence that it stabilizes an open kinase conformation. We selected Ponatinib, which has a K_i for LRRK2 of 31 nM[31], and crystal structures show it bound to RIPK2[32] and IRAK4 (PDB: 6EG9) in open conformations (Extended Data Fig. 9a). Ponatinib inhibited LRRK2^{RCKW}'s ability to phosphorylate Rab8a[13] (Extended Data Fig. 9f).

As our hypothesis predicted, Ponatinib rescued kinesin motility in a dose-dependent manner at concentrations of LRRK2^{RCKW} (25 nM) that had resulted in almost complete inhibition of kinesin (Fig. 5a, Extended Data Fig. 9g-j). We observed similar effects with GZD-824, a chemically-related Type II kinase inhibitor[33] (Fig. 5a and Extended Data Fig. 9i, j). Our hypothesis also predicted that kinase inhibitors that stabilize the closed form of the kinase would not rescue the motors and might enhance the inhibitory effect of LRRK2^{RCKW} by increasing its ability to form filaments on microtubules. Indeed, MLi-2[22,23] and another LRRK2-specific Type I inhibitor, LRRK2-IN-1[34], which are expected[22,35] to stabilize a closed conformation of the kinase (Extended Data Fig. 9b-e), further enhanced the inhibitory activity of LRRK2^{RCKW} on kinesin (Fig. 5a). Dynein motility was also rescued by Ponatinib and GZD-824, but not by MLi-2 or LRRK2-IN-1 (Fig. 5b, Extended Data Fig. 9i, k). Like Ponatinib, GZD-824, MLi-2 and LRRK2-IN-1 inhibited phosphorylation of Rab8a by LRRK2^{RCKW} (Extended Data Fig. 9f).

GZD-824 reduces filaments in cells

In cells, LRRK2 forms filaments that colocalize with a subset of microtubules and are sensitive to the microtubule depolymerizing drug nocodazole[12]. This association is enhanced by the PD-linked mutations R1441C, R1441G, Y1699C and I2020T[12,36] and by Type I kinase inhibitors[34,37]. We tested our kinase conformation hypothesis in human 293T cells by determining if Type I and Type II kinase inhibitors had opposite effects on the formation of microtubule-associated LRRK2 filaments in cells. Consistent with previous findings[37,38], the Type I inhibitor MLi-2 enhanced LRRK2's microtubule association (Fig. 5c), suggesting that the closed conformation of the kinase favours binding to microtubules in cells. In contrast, we found that the Type II inhibitor GZD-824 reduced the filament-forming ability of overexpressed LRRK2 (I2020T) (Fig. 5d). This reduction in LRRK2 filament formation was not due to changes in LRRK2 protein expression levels or the overall architecture of the microtubule cytoskeleton (Extended Data Fig. 9l-n).

Conclusions

Here we reported the 3.5Å structure of the catalytic half of LRRK2 and used it, in combination with a 14Å cryo-ET structure of microtubule-associated LRRK2 filaments[5], to build an atomic model of these filaments. This modelling led us to hypothesize that the conformation of LRRK2's kinase controls its association with microtubules (Fig. 5e). Cryo-EM structures of LRRK2^{RCKW} dimers we obtained in the absence of microtubules showed that the same interfaces are involved in both dimerization and filament formation, and aligning them *in silico* resulted in a right-handed filament with similar properties to LRRK2 filaments observed in cells, suggesting that the ability of LRRK2 to form filaments is a property inherent to LRRK2, and specifically the RCKW domains. We propose that both the surface charge and geometric complementarity between the microtubule and LRRK2 promote the formation of LRRK2 filaments. It remains to be determined whether LRRK2^{RCKW} monomers or dimers are the minimal filament forming unit.

We tested our model that the conformation of LRRK2's kinase regulates microtubule association using kinase inhibitors expected to stabilize either the open (Type II) or closed (Type I) conformations of the kinase. In support of our model, Type II inhibitors relieved the LRRK2^{RCKW}-dependent inhibition of kinesin and dynein and reduced LRRK2 filament formation in cells, while Type I inhibitors failed to rescue motor motility and enhanced filament formation in cells. Importantly, our single-molecule motility assays showed that low nanomolar concentrations of LRRK2^{RCKW} negatively impact both kinesin and dynein. At these low concentrations it is likely that LRRK2 would not form the long, highly ordered filaments and microtubule bundles observed in cells overexpressing the protein; instead, we hypothesize that at endogenous expression levels in cells LRRK2 forms short oligomers on microtubules.

What is the physiological role of non-pathogenic microtubule-associated LRRK2? Our data show that LRRK2 acts as a roadblock for microtubule-based motors in vitro. In cells, dynein and kinesin bind directly or indirectly to many Rab-marked cargos[39–43]. Our data also show that the microtubule-associated form of LRRK2 has its

kinase in a closed (and potentially active) conformation. Given this, microtubule-associated LRRK2 stalling of kinesin or dynein could increase the likelihood that LRRK2 phosphorylates cargo-associated Rabs[13], modulating effector binding[13] and resulting in changes in cargo dynamics. In support of this, the four PD mutations that enhance LRRK2 microtubule binding[12] also show higher levels of Rab phosphorylation in cells than the G2019S mutant[13,14], whose microtubule binding is not enhanced over wild-type LRRK2[12].

Our data have important implications for the design of LRRK2 kinase inhibitors for therapeutic purposes. They predict that inhibitors that favour the closed conformation of the kinase will promote LRRK2 filament formation, thus blocking microtubule-based trafficking, while inhibitors that favour an open conformation of the kinase will not. These results should be taken into account to enhance therapeutically beneficial effects of LRRK2 kinase inhibition and to avoid potential unintended side effects.

Online content

Any methods, additional references, Nature Research reporting summaries, source data, extended data, supplementary information, acknowledgements, peer review information; details of author contributions and competing interests; and statements of data and code availability are available at https://doi.org/10.1038/s41586-020-2673-2.

1. Monfrini, E. & Di Fonzo, A. Leucine-Rich Repeat Kinase (LRRK2) Genetics and Parkinson's Disease. *Adv. Neurobiol.* **14**, 3–30 (2017).
2. Di Maio, R. et al. LRRK2 activation in idiopathic Parkinson's disease. *Sci. Transl. Med.* **10**, (2018).
3. Abeliovich, A. & Gitler, A. D. Defects in trafficking bridge Parkinson's disease pathology and genetics. *Nature* **539**, 207–216 (2016).
4. Gloeckner, C. J. et al. The Parkinson disease causing LRRK2 mutation I2020T is associated with increased kinase activity. *Hum. Mol. Genet.* **15**, 223–232 (2006).
5. Watanabe, R. et al. The in situstructure of Parkinson's disease-linked LRRK2. *bioRxiv* **7**, (2019).
6. Gotthardt, K., Weyand, M., Kortholt, A., Van Haastert, P. J. M. & Wittinghofer, A. Structure of the Roc-COR domain tandem of C. tepidum, a prokaryotic homologue of the human LRRK2 Parkinson kinase. *EMBO J.* **27**, 2239–2249 (2008).
7. Deyaert, E. et al. Structure and nucleotide-induced conformational dynamics of the *Chlorobium tepidum* Roco protein. *Biochem. J.* **476**, 51–66 (2019).
8. Deng, J. et al. Structure of the ROC domain from the Parkinson's disease-associated leucine-rich repeat kinase 2 reveals a dimeric GTPase. *Proc. Natl Acad. Sci. USA* **105**, 1499–1504 (2008).
9. Zhang, P. et al. Crystal structure of the WD40 domain dimer of LRRK2. *Proc. Natl Acad. Sci. USA* **116**, 1579–1584 (2019).
10. Guaitoli, G. et al. Structural model of the dimeric Parkinson's protein LRRK2 reveals a compact architecture involving distant interdomain contacts. *Proc. Natl Acad. Sci. USA* **113**, E4357–E4366 (2016).
11. Sejwal, K. et al. Cryo-EM analysis of homodimeric full-length LRRK2 and LRRK1 protein complexes. *Sci. Rep.* **7**, 8667 (2017).
12. Kett, L. R. et al. LRRK2 Parkinson disease mutations enhance its microtubule association. *Hum. Mol. Genet.* **21**, 890–899 (2012).
13. Steger, M. et al. Phosphoproteomics reveals that Parkinson's disease kinase LRRK2 regulates a subset of Rab GTPases. *eLife* **5**, e12813 (2016).
14. Steger, M. et al. Systematic proteomic analysis of LRRK2-mediated Rab GTPase phosphorylation establishes a connection to ciliogenesis. *eLife* **6**, e31012 (2017).
15. Ito, G. et al. GTP binding is essential to the protein kinase activity of LRRK2, a causative gene product for familial Parkinson's disease. *Biochemistry* **46**, 1380–1388 (2007).
16. West, A. B. et al. Parkinson's disease-associated mutations in LRRK2 link enhanced GTP-binding and kinase activities to neuronal toxicity. *Hum. Mol. Genet.* **16**, 223–232 (2007).
17. Lietha, D. et al. Structural basis for the autoinhibition of focal adhesion kinase. *Cell* **129**, 1177–1187 (2007).
18. Terheyden, S., Ho, F. Y., Gilsbach, B. K., Wittinghofer, A. & Kortholt, A. Revisiting the Roco G-protein cycle. *Biochem. J.* **465**, 139–147 (2015).
19. Cheng, K.-Y. et al. The role of the phospho-CDK2/cyclin A recruitment site in substrate recognition. *J. Biol. Chem.* **281**, 23167–23179 (2006).
20. Pungaliya, P. P. et al. Identification and characterization of a leucine-rich repeat kinase 2 (LRRK2) consensus phosphorylation motif. *PLoS One* **5**, e13672 (2010).
21. Hui, K. Y. et al. Functional variants in the *LRRK2* gene confer shared effects on risk for Crohn's disease and Parkinson's disease. *Sci. Transl. Med.* **10**, eaai7795 (2018).
22. Scott, J. D. et al. Discovery of a 3-(4-Pyrimidinyl) Indazole (MLi-2), an Orally Available and Selective Leucine-Rich Repeat Kinase 2 (LRRK2) Inhibitor that Reduces Brain Kinase Activity. *J. Med. Chem.* **60**, 2983–2992 (2017).
23. Fell, M. J. et al. MLi-2, a Potent, Selective, and Centrally Active Compound for Exploring the Therapeutic Potential and Safety of LRRK2 Kinase Inhibition. *J. Pharmacol. Exp. Ther.* **355**, 397–409 (2015).
24. Case, R. B., Pierce, D. W., Hom-Booher, N., Hart, C. L. & Vale, R. D. The directional preference of kinesin motors is specified by an element outside of the motor catalytic domain. *Cell* **90**, 959–966 (1997).
25. Redwine, W. B. et al. The human cytoplasmic dynein interactome reveals novel activators of motility. *eLife* **6**, e28257 (2017).
26. Dixit, R., Ross, J. L., Goldman, Y. E. & Holzbaur, E. L. F. Differential regulation of dynein and kinesin motor proteins by tau. *Science* **319**, 1086–1089 (2008).
27. Monroy, B. Y. et al. A Combinatorial MAP Code Dictates Polarized Microtubule Transport. *Dev. Cell* **53**, 60–72.e4 (2020).
28. Reck-Peterson, S. L. et al. Single-molecule analysis of dynein processivity and stepping behavior. *Cell* **126**, 335–348 (2006).
29. Qiu, W. et al. Dynein achieves processive motion using both stochastic and coordinated stepping. *Nat. Struct. Mol. Biol.* **19**, 193–200 (2012).
30. DeWitt, M. A., Chang, A. Y., Combs, P. A. & Yildiz, A. Cytoplasmic dynein moves through uncoordinated stepping of the AAA+ ring domains. *Science* **335**, 221–225 (2012).
31. Liu, M. et al. Type II kinase inhibitors show an unexpected inhibition mode against Parkinson's disease-linked LRRK2 mutant G2019S. *Biochemistry* **52**, 1725–1736 (2013).
32. Canning, P. et al. Inflammatory Signaling by NOD-RIPK2 Is Inhibited by Clinically Relevant Type II Kinase Inhibitors. *Chem. Biol.* **22**, 1174–1184 (2015).
33. Ren, X. et al. Identification of GZD824 as an orally bioavailable inhibitor that targets phosphorylated and nonphosphorylated breakpoint cluster region-Abelson (Bcr-Abl) kinase and overcomes clinically acquired mutation-induced resistance against imatinib. *J. Med. Chem.* **56**, 879–894 (2013).
34. Deng, X. et al. Characterization of a selective inhibitor of the Parkinson's disease kinase LRRK2. *Nat. Chem. Biol.* **7**, 203–205 (2011).
35. Gilsbach, B. K. et al. Structural Characterization of LRRK2 Inhibitors. *J. Med. Chem.* **58**, 3751–3756 (2015).
36. Godena, V. K. et al. Increasing microtubule acetylation rescues axonal transport and locomotor deficits caused by LRRK2 Roc-COR domain mutations. *Nat. Commun.* **5**, 5245 (2014).
37. Blanca Ramírez, M. et al. GTP binding regulates cellular localization of Parkinson's disease-associated LRRK2. *Hum. Mol. Genet.* **26**, 2747–2767 (2017).
38. Schmidt, S. H. et al. The dynamic switch mechanism that leads to activation of LRRK2 is embedded in the DFGψ motif in the kinase domain. *Proc. Natl Acad. Sci. USA* **116**, 14979–14988 (2019).
39. Wang, Y. et al. CRACR2a is a calcium-activated dynein adaptor protein that regulates endocytic traffic. *J. Cell Biol.* **218**, 1619–1633 (2019).
40. Etoh, K. & Fukuda, M. Rab10 regulates tubular endosome formation through KIF13A and KIF13B motors. *J. Cell Sci.* **132**, (2019).
41. Horgan, C. P., Hanscom, S. R., Jolly, R. S., Futter, C. E. & McCaffrey, M. W. Rab11-FIP3 links the Rab11 GTPase and cytoplasmic dynein to mediate transport to the endosomal-recycling compartment. *J. Cell Sci.* **123**, 181–191 (2010).
42. Niwa, S., Tanaka, Y. & Hirokawa, N. KIF1Bbeta- and KIF1A-mediated axonal transport of presynaptic regulator Rab3 occurs in a GTP-dependent manner through DENN/MADD. *Nat. Cell Biol.* **10**, 1269–1279 (2008).
43. Matanis, T. et al. Bicaudal-D regulates COPI-independent Golgi-ER transport by recruiting the dynein-dynactin motor complex. *Nat. Cell Biol.* **4**, 986–992 (2002).
44. Sui, H. & Downing, K. H. Structural basis of interprotofilament interaction and lateral deformation of microtubules. *Structure (London, England : 1993)* **18**, 1022–1031 (2010).

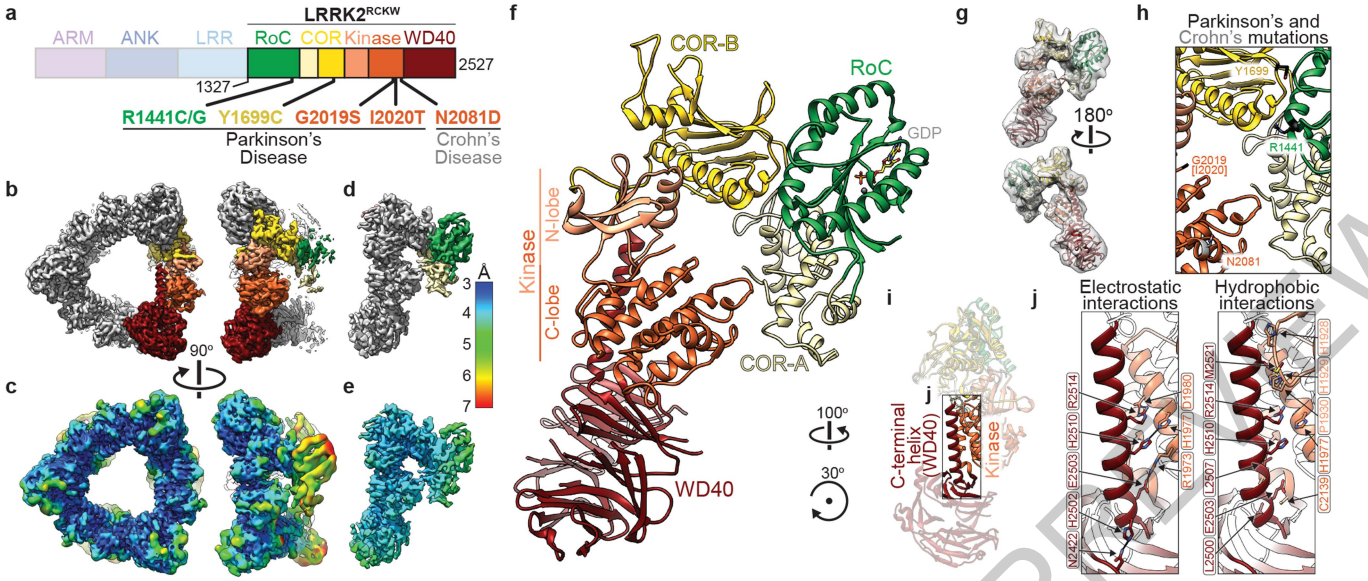

Fig. 1 | Cryo-EM structure of LRRK2^{RCKW}. **a**, Schematic of the construct used in this study. The N-terminal half of LRRK2, absent from our construct, is shown in dim colours. The same colour-coding of domains is used throughout the paper. The five major familial Parkinson's Disease mutations and a Crohn's Disease-linked mutation are indicated. **b**, **c**, 3.5Å cryo-EM map (b) and local resolution (c) of the LRRK2^{RCKW} trimer, with one monomer highlighted. **d**, **e**, 3.8Å cryo-EM map (d) and local resolution (e) of a LRRK2^{RCKW} monomer with improved resolution for the RoC and COR-A domains. **f**, Ribbon diagram of the atomic model of LRRK2^{RCKW}. **g**, 8.1Å cryo-EM map of monomeric LRRK2^{RCKW} with the model in (f) docked in. **h**, Location of the Parkinson's and Crohn's Disease mutations listed in (a). **i**, **j**, Interface between the C-terminal helix and the kinase domain in LRRK2^{RCKW} with residues involved in electrostatic and hydrophobic interactions indicated.

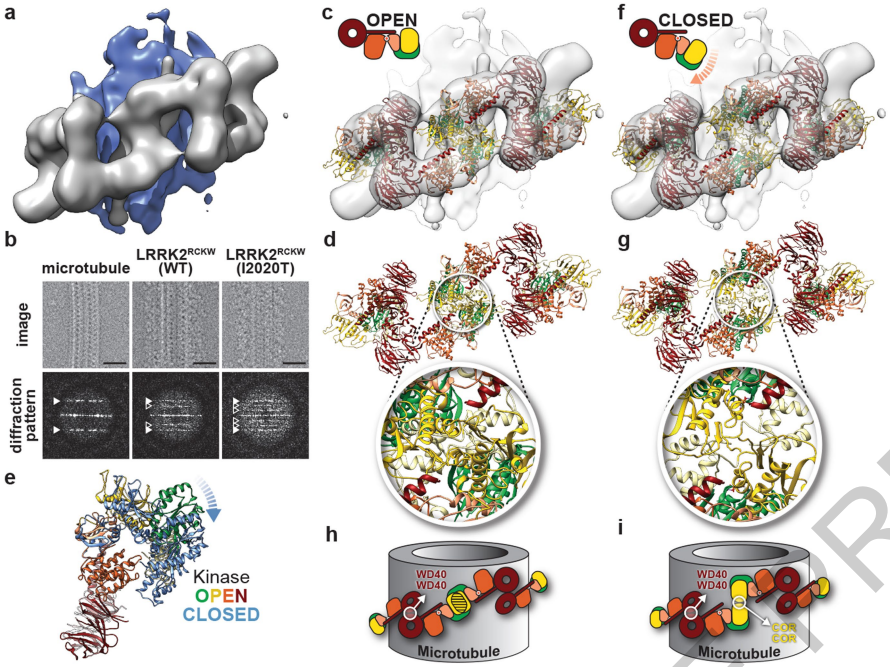

Fig. 2 | Modelling the microtubule-associated LRRK2 filaments. a, 14Å cryo-ET map of a segment of microtubule-associated LRRK2 filament in cells. The microtubule is shown in blue and the LRRK2 filament in grey. **b**, Microtubule-associated LRRK2^{RCKW} filaments reconstituted in vitro from purified components. (Top) Single cryo-EM images of a naked microtubule (left), and WT (centre) and I2020T (right) LRRK2^{RCKW} filaments. (Bottom) Diffraction patterns (power spectra) calculated from the images above. White and hollow arrowheads indicate the layer lines corresponding to the microtubule and LRRK2^{RCKW}, respectively. Scale bar: 20nm **c**, Fitting of the LRRK2^{RCKW} structure, which has its kinase in an open conformation, into the cryo-ET map. **d**, Atomic model of the LRRK2^{RCKW} filaments from (c). The white circle highlights the filament interface mediated by interactions between COR domains, where clashes are found. **e**, Superposition of the LRRK2^{RCKW} structure (colored by domains) and a model of LRRK2^{RCKW} with its kinase in a closed conformation in blue. The dashed blue arrow indicates the closing of the kinase. **f**, Fitting of the closed-kinase model of LRRK2^{RCKW} into the cryo-ET map. **g**, Atomic model of the closed-kinase LRRK2^{RCKW} filaments (g) with a white circle highlighting the same interface as in (d). **h, i**, Cartoon representation of the two filament models, highlighting the clashes observed with open-kinase LRRK2^{RCKW} (h) and resolved with the closed-kinase model (i). 82% of clashes were resolved using the closed-kinase LRRK2^{RCKW} model (see Methods for details).

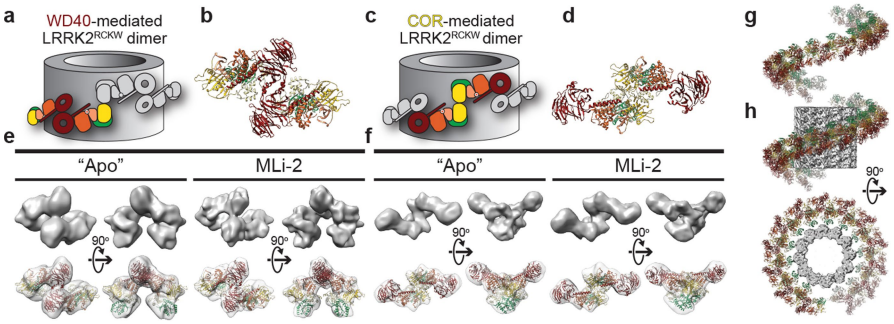

Fig. 3 | LRRK2^{RCKW} forms WD40- and COR-mediated dimers outside the filaments. a-d, The filament model shown in Fig. 2j, k is shown here in grey, with either a WD40-mediated (a), or COR-mediated (c) LRRK2^{RCKW} dimer highlighted with domain colours. The corresponding molecular models are shown next to the cartoons (b, d). **e, f**, Cryo-EM reconstructions of LRRK2^{RCKW} dimers obtained in the absence of inhibitor ("Apo"), or in the presence of MLi-2. For each reconstruction, two orientations of the map are shown: down the twofold axis at the dimerization interface (left), which matches the orientation of the models shown in (b, d), and perpendicular to it (right). The top row shows the cryo-EM map and the bottom row a transparent version of it with a model docked in. **g**, Molecular models of the WD40-mediated and COR-mediated LRRK2^{RCKW} dimers obtained in the presence of MLi-2 (e, f) were aligned in alternating order. This panel shows the resulting right-handed helix. **h**, The helix has dimensions compatible with the diameter of a 12-protofilament microtubule (EMD-5192)[44], which was the species used to obtain the cryo-ET map shown in Fig. 2a [5], and has its RoC domains pointing towards the microtubule surface.

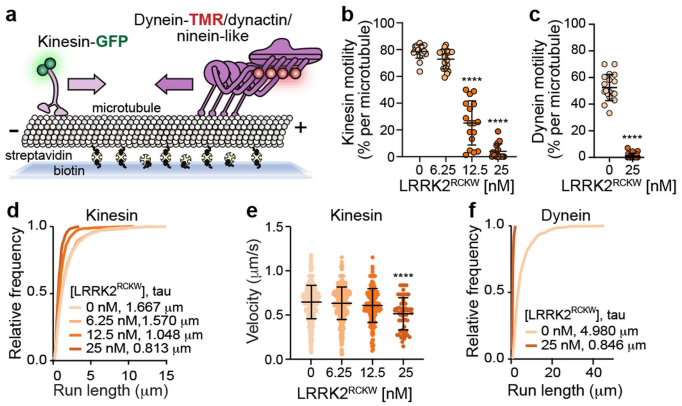

Fig. 4 | LRRK2^{RCKW} inhibits the motility of kinesin and dynein. a, Schematic of the single-molecule motility assay. **b**, **c**, The percentage (mean ± s.d.) of motile events per microtubule as a function of LRRK2^{RCKW} concentration for kinesin (b) and dynein (c). ****$P < 0.0001$ (Kruskal–Wallis test with Dunn's posthoc for multiple comparisons for (b)) and ****$P < 0.0001$ (Mann–Whitney test) for (c)). **d**, Cumulative frequency distribution of kinesin run lengths as a function of LRRK2^{RCKW} concentration. Mean decay constants (tau) are shown. The 12.5 nM and 25 nM, but not 6.25 nM, conditions were significantly different ($P < 0.0001$) than the 0 nM condition (one-way ANOVA with Dunnett's test for multiple comparisons using error generated from a bootstrapping analysis). **e**, Velocity of kinesin as a function of LRRK2^{RCKW} concentration. Data are mean ± s.d. ****$P < 0.0001$ (one-way ANOVA with Dunn's posthoc for multiple comparisons). **f**, Cumulative frequency distribution of dynein run lengths as a function of LRRK2^{RCKW} concentration. Mean decay constants (tau) are shown. Data was resampled with bootstrapping analysis and was significant. $P < 0.0001$ (unpaired *t*-test with Welch's correction using error generated from a bootstrapping analysis).

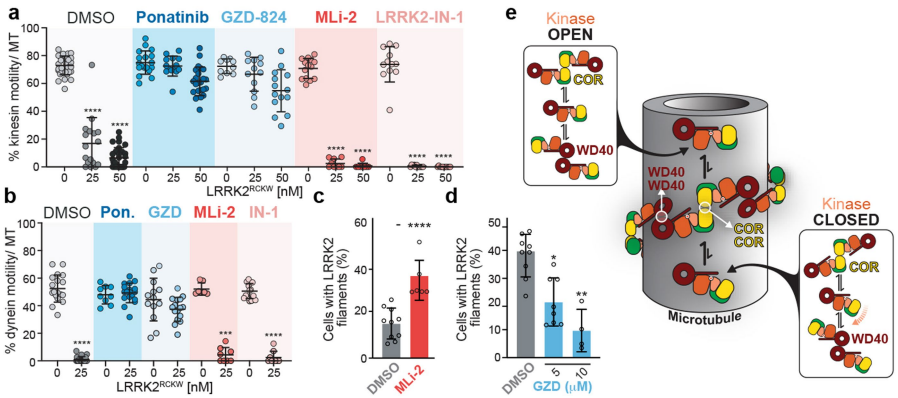

Fig. 5 | Type II, but not Type I, kinase inhibitors rescue kinesin and dynein motility and reduce LRRK2 filament formation in cells. a, b, Effects of different kinase inhibitors on LRRK2^{RCKW}'s inhibition of kinesin (a) and dynein (b) motility. Data shown is the percentage of motile events per microtubule (MT) as a function of LRRK2^{RCKW} concentration in the absence (DMSO) or presence of the indicated inhibitors (Ponatinib and GZD-824: 10 μM; MLi-2 and LRRK2-IN-1: 1 μM). Data are mean ± s.d. ***P < 0.001 and ****P < 0.0001 (Kruskal–Wallis test with Dunn's posthoc for multiple comparisons within drug only). **c**, Treatment with MLi-2 (500 nM) for 2 h increases WT GFP-LRRK2 filament formation in 293T cells. Data are mean ± s.d. ****P = 0.0002 (Mann–Whitney test). **d**, Treatment with GZD-824 (5 μM) for 30 min decreases GFP-LRRK2 (I2020T) filament formation in 293 cells. Data are mean ± s.d. *P = 0.0133 and **P = 0.0012 (Kruskal–Wallis with Dunn's posthoc test for multiple comparisons). **e**, Schematic representation of our hypothesis. LRRK2's kinase can be in an open or closed conformation. The different species we observed are represented in the rounded rectangles, but only monomers are shown on the microtubule for simplicity. Our model proposes that the kinase-closed form of LRRK2 favours oligomerization on microtubules.

Methods

Cloning, plasmid construction, and mutagenesis

For baculovirus expression, the DNA coding for wild-type LRRK2 residues 1327 to 2527 (taken from Mammalian Gene Collection) was PCR-amplified using the forward primer TACTTCCAATCCATGAAAA AGGCTGTGCCTTATAACCGA and the reverse primer TATCCACCTTT ACTGTCACTCAACAGATGTTCGTCTCATTTTTTCA. The T4 polymerase-treated amplicon was inserted into the expression vector pFB-6HZB by ligation-independent cloning. According to Bac-to-Bac expression system protocols (Invitrogen), this plasmid was used for the generation of recombinant Baculoviruses.

For mammalian expression vectors, pDEST53-GFP-LRRK2 (WT)[62] from Addgene (#25044) was used. pDEST53-GFP-LRRK2 (I2020T) was cloned using QuikChange site-directed mutagenesis (Agilent) with the forward primer AAGATTGCTGACTACGGCACTGCTCAGTACTGCTG and the reverse primer CAGCAGTACTGAGCAGTGCCGTAGTCAGCAATCTT. pET17b-Kif5b(1-560)-GFP-His[47] was obtained from Addgene (#15219). For pET28a-ZZ-TEV-Halo-NINL$^{1\text{-}702}$, Ninein-like$^{1\text{-}702}$ (NINL) was synthesized as previously described[25] and inserted into a pET28a expression vector with a synthesized ZZ-TEV-Halo gBlock fragment (IDT) using Gibson assembly.

LRRK2^{RCKW} expression and purification

The expression construct contained an N-terminal His_6-Z-tag, cleavable with TEV protease (Extended Data Fig. 1a-c). For LRRK2^{RCKW} purification, the pelleted Sf9 cells were washed with PBS, resuspended in lysis buffer (50 mM HEPES pH 7.4, 500 mM NaCl, 20 mM imidazole, 0.5 mM TCEP, 5% glycerol, 5 mM $MgCl_2$, 20 μM GDP) and lysed by sonication. The lysate was cleared by centrifugation and loaded onto a Ni-NTA (Qiagen) column. After vigorous rinsing with lysis buffer the His_6-Z-tagged protein was eluted in lysis buffer containing 300 mM imidazole. Immediately thereafter, the eluate was diluted with a buffer containing no NaCl, in order to reduce the NaCl-concentration to 250 mM and loaded onto an SP sepharose column. His_6-Z-TEV-LRRK2^{RCKW} was eluted with a 250 mM to 2.5 M NaCl gradient and treated with TEV protease overnight to cleave the His_6-Z-tag. Contaminating proteins, the cleaved tag, uncleaved protein and TEV protease were removed by another combined SP sepharose Ni-NTA step. Finally, LRRK2^{RCKW} was concentrated and subjected to gel filtration in storage buffer (20 mM HEPES pH 7.4, 800 mM NaCl, 0.5 mM TCEP, 5% glycerol, 2.5 mM $MgCl_2$, 20 μM GDP) using an AKTA Xpress system combined with an S200 gel filtration column. The final yield as calculated from UV absorbance was 1.2 mg LRRK2^{RCKW}/L insect cell medium.

SEC-MALS

SEC-MALS experiments were performed using an ÄKTAmicro chromatography system hooked up to a Superdex 200 Increase 3.2/300 size exclusion chromatography column coupled in-line to a DAWN HELEOS II multiangle light scattering detector (Wyatt Technology) and an Optilab T-rEX refractive index detector (Wyatt Technology). SEC-MALS was performed in 50 mM Hepes pH 7.4, 200 mM NaCl 0.5 mM TCEP, 5% glycerol, 5 mM MgCl2, and 20 μM GDP. For a typical sample, 50 uL of ~7 μM LRRK2^{RCKW} was injected onto the column. Molar mass was calculated using ASTRA 6 software, with protein concentration derived from the Optilab T-rEX. LRRK2^{RCKW} used for SEC-MALS experiments contained an extra 16 residue N-terminal Gly-Ser linker sequence.

Electron microscopy

Electron microscopy sample preparation and imaging of trimer data set. Purified LRRK2^{RCKW} was dialysed into a final buffer consisting of 20mM HEPES pH7.4, 80mM NaCl, 0.5mM TCEP, 5% glycerol, 2.5mM $MgCl_2$ and 20μM GDP and then diluted to a final concentration of 4μM in the same buffer. We have only observed the trimer species when preparing grids with LRRK2^{RCKW} at concentrations of 4μM or above and for our "Apo" samples (that is, in the absence of inhibitors). This sample was applied to glow-discharged (20mA for 20 s in a K100 Instrument) UltrAuFoil Holey Gold R1.2/1.3 grids (Quantifoil). A Vitrobot (FEI) was then used to blot away excess sample and plunge freeze the grids in liquid ethane. Grids were stored in liquid nitrogen until imaged.

Cryo-EM data was collected at UCLA California NanoSystems Institute in a Titan Krios (FEI) operated at 300kV, equipped with a K2 Summit direct electron detector (Gatan) and a Quantum energy filter (Gatan). Automated data collection was performed using Leginon[48]. We recorded a total of 3,824 movies in 'counting mode' at a dose rate of 6.65 electrons $Å^{-2}$ sec^{-1} with a total exposure time of 8 s sub-divided into 200ms frames, for a total of 40 frames. The images were recorded at a nominal magnification of 130,000x resulting in an object pixel size of 1.07Å. The defocus range of the data was -1μm to -1.8μm.

Electron microscopy map and model generation of trimer data set. We aligned the movie frames using UCSF MotionCor2[49], using the dose-weighted frame alignment option. We estimated the CTF on dose-weighted images using GCTF version 1.06[63] as implemented in Appion[50] with per-particle CTF generation. Images having CTF fits worse that 5Å (as determined by GCTF) were excluded from further processing. Using this approach, 3,693 micrographs were kept for further processing. We selected particles from micrographs using FindEM[51] with projections of a trimeric LRRK2^{RCKW} map, created from an initial Cryosparc ab initio model generation, serving as a reference. Particle picking was performed within the framework of Appion, resulting in a data set of 836,956 particles.

We carried out subsequent processing first in Relion 3.0[52] then in CryoSparc2[53]. A series of 2D and 3D classifications were performed as shown in Extended Data Fig. 1f to generate the final map. The initial reference was created in a similar manner to those used for template picking, from an initial ab initio model generated in CryoSparc. All references were filtered to either 60Å (default in Relion) or 30Å (default in CryoSparc) before refinement processes. The final map, generated in Cryosparc2 using non-uniform refinement and while applying C3 symmetry, reached 3.47Å resolution. Initial 2D classifications used binned data (4.28Å $pixel^{-1}$) while all subsequent 3D classifications and refinement steps used unbinned images (1.07Å $pixel^{-1}$).

In order to improve the density corresponding to the RoC and COR-A domains, a second map was generated following a different processing scheme, which used signal subtraction and is shown in Extended Data Fig. 2a. The final refinement led to a 3.8Å map of LRRK2^{RCKW}. All the steps used unbinned images (1.07Å $pixel^{-1}$).

The resolutions of the cryo-EM maps, here and below, were estimated from Fourier Shell Correlation (FSC) curves calculated using the gold-standard procedure and the resolutions are reported according to the 0.143 cutoff criterion[54–56]. FSC curves were corrected for the convolution effects of a soft mask applied to the half maps by high-resolution phase randomization[57]. For display and analysis purposes, we sharpened the maps with automatically estimated negative B factors from Relion or CryoSparc2.

We built the LRRK2^{RCKW} models using both the 3.47Å C3 and 3.8Å density-subtracted maps. We used a combination of Rosetta[58] and manual building in Coot[59] to build all models. Starting models were found via a sequence alignment search in HHpred[60] and each section was built from the following: (1) The RoC and COR domains were built using the top two alignment results, 3DPT_B and 3DPU_B, which scored much higher than those ranked third and below; (2) The kinase N-lobe, kinase C-lobe, and WD40 domain were all built from the top five sequence matches: 5JGA_A, 1OPK_A, 4BTF_A, 5GZA_A, 5K00_A for the kinase N-lobe; 5CYZ_A, 2IZR_A, 5YKS_B, 3S95_B, 4TWC_B for the kinase C-lobe; and 4J87_A, 3OW8_C, 5U69_A, 5O9Z_F, 5T2A_7 for the WD40 domain. The C-terminal helix was built manually. We built the COR-B, KIN, and WD40 domains using the density of the 3.47Å C3 map and the RoC and COR-A domains using the 3.8Å map, then connected the two

after fitting them into the 3.8Å map. Finally, we performed multiple iterations of both the CM and Relax functions in Rosetta, along with manual manipulation in Coot, to build our final 20 models (10 including GDP-Mg^{2+} in the RoC domain, and 10 excluding it). In areas of weak density, we either removed part of the polypeptide chain or, where only side chain density was poor, converted the chain to poly-alanine.

The GDP-Mg^{2+} was placed in our model by initially aligning a structure of the RoC domain containing a bound GDP-Mg^{2+} (PDB: 2zej)[8] to the RoC domain in our structure. The GDP-Mg^{2+} was then added to our model in the aligned position and run through Rosetta to allow for fine movements into our density and re-arrangement of nearby chains.

The phosphorylation of the threonine residue 1343, which we observe in our map and is a known phosphorylation site of Roco family GTPases[61], was confirmed by phosphor-enrichment mass spec (data not shown).

Electron microscopy sample preparation, imaging, and processing of apo, MLi2, Ponatinib LRRK2^{RCKW} monomer/dimers. For all samples, purified LRRK2^{RCKW} was dialysed into the same final buffer as described for the trimer data, then diluted to its final concentration in the same buffer. Unlike with the trimer data, however, the following data sets were collected from multiple grids prepared using slightly different sample conditions and imaged using a range of microscope settings.

The apo LRRK2^{RCKW} monomer data set had sample diluted to final concentrations ranging between 1µm and 6µm. In addition, one data set was collected with the grid tilted to 30° to overcome preferred orientation issues. Otherwise, grids were prepared as described for the trimer data set.

The apo LRRK2^{RCKW} dimer data set had sample diluted to final concentrations ranging between 4µM and 12µM. Two of the samples contained 0.05mM Digitonin (Sigma, D141) or 0.03% octyl glucoside (Sigma, O8001) detergents to overcome preferred orientation issues. One data set was collected with the grid tilted to 30°, also to overcome preferred orientation issues. Otherwise, grids were prepared as described for the trimer data set.

The MLi-2 LRRK2^{RCKW} dimer data set had sample diluted to final concentrations of either 3µM or 4µM. MLi-2 was added post-dialysis to a final concentration of 5µM. The sample was incubated on ice for at least one hour before being applied to the grid. Otherwise, grids were prepared as described for the trimer data set.

The ponatinib LRRK2^{RCKW} dimer data set had sample diluted to final concentrations of 2µM or 4µM. Ponatinib was added post-dialysis at a concentration of either 5µM or 100uM. The sample was incubated on ice for at least one hour before being applied to the grid. Otherwise, grids were prepared as described for the trimer data set.

The apo LRRK2^{RCKW} monomer cryo-EM data was collected on a Talos Arctica (FEI) operated at 200kV, equipped with a K2 Summit direct electron detector (Gatan). Automated data collection was performed using Leginon[48]. A total of 11,354 movies were collected. We imaged samples at dose rates between 4.2 and 10 electrons $Å^{-2}$ sec^{-1} with total exposure times ranging from 6 s to 12 s sub-divided into 200ms frames, for a total of 30 or 60 frames. All the images were recorded at a nominal magnification of 36,000x (either counting mode or super resolution mode) resulting in object pixel sizes of either 1.16Å or 0.58Å, respectively. The defocus range of the data was -1µm to -2µm.

Frame alignment, CTF estimation and image selection were performed as described for the trimer data set except that per-particle CTF was not used, instead the CTF information of the whole image was used. After selection we had 7,067 micrographs. Particles were extracted using crYOLO[62]. We carried out subsequent processing in CryoSparc2[53] on binned images (2.32Å $pixel^{-1}$).

A series of 2D and 3D classifications were performed as shown in Extended Data Fig. 6 to generate the final map. The initial monomer reference, used for refinement of the monomer map, was generated from our LRRK2^{RCKW} model. The initial dimer references, used for particle sorting, were generated as shown in Extended Data Fig. 5a-e. All references were filtered to 30Å, the default value in CrypSparc2, before refinement processes. This final map reached a resolution of 8.08Å using non-uniform refinement.

The apo LRRK2^{RCKW} dimer cryo-EM data was collected as described for the apo LRRK2^{RCKW} monomer. A total of 5,303 movies were collected. We imaged samples at dose rates between 4.6 and 7.8 electrons $Å^{-2}$ sec^{-1} with total exposure times ranging between 7 s and 11 s sub-divided into 200ms frames, for a total of 35 or 55 frames. All the images were recorded at a nominal magnification of 36,000x (either counting mode or super resolution mode) resulting in object pixel sizes of either 1.16Å or 0.58Å, respectively. The defocus range of the data was -1µm to -2µm.

Frame alignment, CTF estimation, image selection, and particle picking were performed as described for the apo LRRK2^{RCKW} monomer. After selection we had 3,100 micrographs. We carried out subsequent processing in CryoSparc2[53] on binned images (2.32Å $pixel^{-1}$).

The classification and refinement scheme for the apo LRRK2^{RCKW} WD40- and COR-mediated dimer maps is shown in Extended Data Fig. 6. The same initial dimer references used for the apo LRRK2^{RCKW} monomer, filtered to the same resolution, were used here for refinement of the dimer maps. In addition, a linear trimer reference, generated by combining two initial dimer references and filtered to the same resolution, was used during the initial 3D classification step to sort out species longer than dimer, which negatively affected subsequent alignment. The final maps had resolutions of 13.39Å (WD40-mediated dimer) and 9.52Å (COR-mediated dimer) with C2 symmetry applied to both.

The MLi-2 LRRK2^{RCKW} dimer cryo-EM data was collected as described for the apo LRRK2^{RCKW} monomer. We recorded a total of 4,139 movies. We imaged all data sets in 'counting mode' at a dose rate of 5.5 electrons $Å^{-2}$ sec^{-1}, with total exposure times of either 9 s or 10 s sub-divided into 200ms frames, for a total of 45 or 50 frames. All the images were recorded at a nominal magnification of 36,000x (counting mode) resulting in object pixel sizes of 1.16Å. The defocus range of the data was -1µm to -2µm.

Frame alignment, CTF estimation, image selection, and particle picking were performed as described for the apo LRRK2^{RCKW} monomer. After selection, 4,030 micrographs were kept for further processing. Processing was done in Relion 3.0[52] then CryoSparc2[53] using binned images (2.32Å $pixel^{-1}$).

The classification and refinement scheme for the MLi-2 LRRK2^{RCKW} WD40- and COR-mediated dimer maps is shown in Extended Data Fig. 5. The same references used for the apo LRRK2^{RCKW} dimers, and filtered to the same resolution, were used here for the same purposes. The final maps had resolutions of 9.74Å (WD40-mediated dimer) and 9.04Å (COR-mediated dimer), with no symmetry applied.

The Ponatinib LRRK2^{RCKW} dimer cryo-EM data was collected as described for the apo LRRK2^{RCKW} monomer. We recorded a total of 1,797 movies. We imaged all data sets at dose rates of either 5.5 or 9.7 electrons $Å^{-2}$ sec^{-1} with total exposure times of 7 s or 10 s sub-divided into 200ms frames, for a total of 35 or 50 frames. All the images were recorded at a nominal magnification of 36,000x (counting mode) resulting in object pixel sizes of 1.16Å. The defocus range of the data was -1µm to -2µm.

Frame alignment, CTF estimation, image selection, and particle picking were performed as described for the apo LRRK2^{RCKW} monomer. 1,455 micrographs were kept for further processing. Processing was done in CryoSparc2[53] on binned images (2.32Å $pixel^{-1}$). Ponatinib LRRK2^{RCKW} dimer particles were sorted via 2D classification leading to the final 2D averages shown in Extended Data Fig. 6b.

Electron microscopy sample preparation and imaging of microtubule-associated LRRK2^{RCKW}. Purified LRRK2^{RCKW} and unpolymerized bovine tubulin were added together to the microtubule

polymerization buffer (1x BRB80, 1mM DTT, 10% DMSO, 1mM GTP, 1mM MgCl2, 10μM Taxol). LRRK2^{RCKW} was added in a 2X molar excess relative to the α/β tubulin dimer during the polymerization procedure. To promote LRRK2^{RCKW}'s interaction with microtubules, NaCl concentration was capped at 90mM; this set an upper limit to the LRRK2^{RCKW} concentrations we could use. For wild-type LRRK2^{RCKW} we used 2.5μM LRRK2^{RCKW} and 1.25μM tubulin. For the I2020T variant we used 4.5μM LRRK2^{RCKW} (I2020T) and 2.25μM tubulin, respectively. The mixture was incubated for 1 h at room temperature and was then diluted threefold into cryo-EM buffer (20mM HEPES pH 7.4, 80mM NaCl, 0.5mM TCEP, 2.5mM MgCl2, 10μM Taxol) immediately before application to the grid and plunge-freezing in a Vitrobot (FEI). The grids (Lacey Carbon on copper, 300 mesh; EMS) were glow-discharged (20mA for 40 s in a K100 Instrument) before the sample was applied.

Cryo-EM data was collected on a Talos Arctica (FEI) operated at 200kV, equipped with a K2 Summit direct electron detector (Gatan) using Leginon[48]. We imaged at a dose rate of 5.85 electrons Å^{-2} sec^{-1} with a total exposure time of 10 s sub-divided into 200ms frames, for a total of 50 frames. All the images were recorded at a nominal magnification of 36,000x resulting in an object pixel size of 1.16Å. The defocus range of the data was -1μm to -2μm. Images were aligned using MotionCor2[49] with the dose-weighted frame alignment option.

For layer line analysis, filaments were selected and extracted into 600Å boxes using Relion 3.0[52] from the dose-corrected images. The images were binned fourfold into a pixel size of 4.64Å and a final box size of 164 pixels. Prior to calculating the Fourier transforms, the images were padded with an additional 82 pixels on all sides.

Building the molecular model of microtubule-associated LRRK2^{RCKW} filaments

Given that the WD40 densities are clearly identifiable in the cryo-ET map of microtubule (MT)-associated LRRK2, we used these as a starting point for docking the structure of LRRK2^{RCKW} into the cryo-ET map. First, a synthetic dimer of the WD40 domains from the LRRK2^{RCKW} structure was generated by aligning them to a crystal structure of the isolated WD40 domain, which formed a dimer in the crystal (PDB: 6DLP)[9]. This synthetic dimer was then docked into the cryo-ET map in Chimera[45], using the Fit in Map function with the options of filtering the structure to the resolution of the map (14Å) and optimizing correlation. A WD40 dimer was placed into each of the two corresponding densities present in the map. Then, four copies of the LRRK2^{RCKW} structure were added by aligning their WD40 domains to those previously docked into the cryo-ET map. The same procedure was followed to build the filament using the "closed" kinase model of LRRK2^{RCKW} (see section below for how that model was generated).

Backbone clashes at the COR-mediated interface in the model filament were measured in Chimera[45] (with default settings) after converting the four LRRK2^{RCKW} monomers to poly-alanine models.

Modelling a "closed" kinase version of LRRK2^{RCKW}

In order to identify a good reference to model the closed state of LRRK2^{RCKW}'s kinase, we ran separate structural searches (using the DALI server) with the N- and C-lobes of LRRK2^{RCKW}'s kinase domain. We looked through the matches for a kinase that scored highly with both lobes, and whose structure is in a closed state. We selected Interleukin-2 inducible T-cell kinase (Itk) bound to an inhibitor as our reference (PDB: 3QGY)[46].

LRRK2^{RCKW} was split at the junction between the N- and C-lobes of its kinase domain (L1949-A1950), resulting in one half containing the RoC, COR, and kinase (N-lobe) domains and another containing the kinase (C-lobe) and WD40 domains. The C-lobe of 3QGY was then aligned (in Chimera) to the C-lobe of LRRK2^{RCKW}'s kinase domain, and subsequently the N-lobe of LRRK2^{RCKW}'s kinase was aligned to the N-lobe of 3QGY. The two halves were then combined to generate the "closed" kinase model of LRRK2^{RCKW}.

Docking of LRRK2^{RCKW} into cryo-EM maps of monomers and dimers

In order to build models of WD40- and COR-mediated dimers of LRRK2^{RCKW} in the presence of MLi-2, we again split LRRK2^{RCKW} at the junction between the N- and C-lobes (L1949-A1950). The two halves were fitted into one half of the cryo-EM map of a WD40-mediated dimer of LRRK2^{RCKW} obtained in the presence of MLi-2 (we chose this map as its resolution was higher than that of the COR-mediated dimer). We also docked the two halves of LRRK2^{RCKW} into a cryo-EM map of a LRRK2^{RCKW} monomer obtained in the absence of inhibitor. The fitting was done in Chimera[45] using the Fit in Map function with the options of filtering the structure to the resolution of the map and optimizing correlation. The two halves were then joined to generate a full model of LRRK2^{RCKW}.

The WD40- and COR-mediated dimers of LRRK2^{RCKW} in the presence of MLi-2 were built by docking the models built above into the corresponding cryo-EM maps, using the same approach in Chimera[45] as outlined above.

The LRRK2^{RCKW} "filament" shown in Extended Data Fig. 7f was generated by aligning, in alternating order, multiple copies of the two dimer models (WD40- and COR-mediated) built into the cryo-EM maps obtained in the presence of MLi-2.

Kinase inhibitors

Stocks of the kinase inhibitors MLi-2 (10 mM; Tocris), Ponatinib (10 mM; ApexBio), GZD-824 (10 mM; Cayman Chemical), and LRRK2-IN-1 (2 mM; Michael J Fox Foundation) were stored in DMSO at -20 C.

Antibodies

All antibodies used for immunocytochemistry were diluted to 1:500. Primary antibodies used were chicken anti-GFP (Aves Labs) and rabbit anti-alpha-tubulin (ProteichTech). Secondary antibodies used were goat anti-chicken-Alexa 488 (ThermoFisher) and goat anti-chicken Alexa568 (ThermoFisher). DAPI was used at 1:5000 according to the manufacturers suggestions (ThermoFisher). Primary antibodies used for western blots were mouse anti-GFP (Santa Cruz, 1:1000 dilution) mouse anti-GAPDH (ProteinTech, 1:5000 dilution) and mouse anti-gamma-tubulin (ProteinTech, 1:5000 dilution). Secondary antibodies (1:15,000) used for western blots were IRDye goat anti-mouse 680RD and IRDye goat anti-rabbit 780RD (Li-COR).

Rab8a expression and purification

N-terminally tagged (His_6-ZZ) Rab8a containing a TEV cleavage site was cloned into a PET28a expression vector and expressed in BL21(DE3) *E. coli* cells. Transformed cells were grown overnight at 37 °C in 10 mL LB medium containing kanamycin (50 μg/ml), then diluted into 200 mL LB medium containing kanamycin (50 μg/ml), grown to an optical density at 600 nm of ~1-2, diluted into 4 L LB medium containing kanamycin (50 μg/ml), and grown to an optical density at 600 nm of 0.4. IPTG was added (final concentration 0.5 mM) to induce protein expression for ~18 h at 18 °C. Cells were harvested by centrifugation at 8983 × g for 10 min at 4 °C, followed by resuspension in 15 mL LB medium and centrifugation at 2862 × g for 10 min at 4 °C. The cell pellet was flash frozen in liquid nitrogen and stored at -80 °C. For a typical protein purification, cell pellets were resuspended in lysis buffer (50 mM HEPES pH 7.4, 200 mM NaCl, 2 mM DTT, 10% glycerol, 5 mM $MgCl_2$, 0.5 mM Pefabloc, and protease inhibitor cocktail tablets) and lysed by sonication on ice. The lysate was clarified by centrifugation at 164,700 × g for 40 min at 4 °C and then incubated with Ni-NTA agarose beads (Qiagen) for 1 h at 4 °C. Beads were extensively washed with wash buffer (50 mM HEPES pH 7.4, 150 mM NaCl, 2 mM DTT, 10% glycerol, 5 mM $MgCl_2$); His_6-ZZ-Rab8a was eluted in 40 mL elution buffer (50 mM HEPES pH 7.4, 150 mM NaCl, 300 mM imidazole, 2 mM DTT, 10% glycerol, 5 mM $MgCl_2$). The protein eluate was diluted twofold in wash buffer, incubated with IgG sepharose 6 fast flow beads equilibrated in wash buffer, incubated at 4 °C for

2.5 h, and washed extensively in wash buffer. Protein-bound IgG beads were then transferred into TEV buffer (50 mM HEPES pH 7.4, 200 mM NaCl, 2 mM DTT, 10% glycerol, 5 mM $MgCl_2$), and untagged Rab8a was cleaved off of IgG sepharose beads by incubation with TEV protease at 4 °C overnight. The next day, cleaved Rab8a was separated from His_6-TEV protease and any remaining uncleaved protein or residual tag by incubation with Ni-NTA agarose beads (Qiagen), followed by washing with TEV buffer containing 25 mM imidazole. Lastly, purified Rab8a was run over a Superdex 200 increase 10/300 size exclusion column equilibrated in S200 buffer (50 mM HEPES pH 7.4, 200 mM NaCl, 2 mM DTT, 1% glycerol, 5 mM $MgCl_2$), and concentrated and exchanged into buffer containing 10% glycerol for storage at -80 °C.

In vitro phosphorylation of Rab8a by LRRK2^{RCKW}

Purified Rab8a (~3.8 µM) was phosphorylated by LRRK2^{RCKW} (~38 nM) in a buffer containing 50 mM HEPES pH 7.4, 80 mM NaCl, 10 mM $MgCl_2$, 0.5 mM TCEP, 1 mM ATP, 200 µM GDP); 34 µL reaction mixtures containing kinase inhibitor or an equivalent volume DMSO were incubated at 30 °C, and samples were taken at 45 min, and 90 min. An effective reaction volume of 0.75 µL was run on a 4–12% Bis-Tris protein gel, transferred to nitrocellulose, and blotted with a commercially available antibody to pT72-Rab8a (MJFF-pRab8) as previously described[63] and per manufacturer's instructions, with the exception that HRP-labelled secondary antibody was used at a dilution of 1:2000.

Purification of molecular motors

Protein purification steps were done at 4 °C unless otherwise indicated. Human KIF5B$^{1-560}$ (K560)-GFP was purified from *E. coli* using an adapted protocol previously described[64]. pET17b-Kif5b(1-560)-GFP-His was transformed into BL-21[DE3] RIPL cells (New England Biolabs) until OD 0.6-0.8 and expression was induced with 0.5 mM IPTG for 16 h at 18 °C. Frozen pellets from 2 L culture were resuspended in 40 mL lysis buffer (50 mM Tris, 300 mM NaCl, 5 mM $MgCl_2$, and 0.2 M sucrose, pH 7.5) supplemented with 1 cOmplete EDTA-free protease inhibitor cocktail tablet (Roche) per 50 mL and 1 mg/mL lysozyme. The resuspension was incubated on ice for 30 min and lysed by sonication. Sonicate was supplied with 10 mM imidazole and 0.5 mM PMSF and clarified by centrifuging at 30,000 × g for 30 min in Type 70 Ti rotor (Beckman). The clarified supernatant was incubated with 5 mL Ni-NTA agarose (Qiagen) and rotated in a nutator for 1 h. The mixture was washed with 30 mL wash buffer (50 mM Tris, 300 mM NaCl, 5 mM $MgCl_2$, 0.2 M sucrose, and 20 mM imidazole, pH 7.5.) by gravity flow. Beads were resuspended in elution buffer (50 mM Tris, 300 mM NaCl, 5 mM $MgCl_2$, 0.2 M sucrose, and 250 mM imidazole, pH 8.0), incubated for 5 min, and eluted stepwise in 0.5 mL increments. Peak fractions were combined and buffer exchanged on a PD-10 desalting column (GE Healthcare) equilibrated with storage buffer (80 mM PIPES, 2 mM $MgCl_2$, 1 mM EGTA, and 0.2 M sucrose, pH 7.0). From this, peak fractions of motor solution were either flash frozen at -80 °C until further use or immediately subjected to microtubule bind and release purification. A total of 1 mL motor solution was incubated with 1 mM AMP-PNP and 20 µM taxol on ice for 5 min and warmed to room temperature (RT). For microtubule bind and release, polymerized bovine brain tubulin was centrifuged through a glycerol cushion (80 mM PIPES, 2 mM $MgCl_2$, 1 mM EGTA, and 60% glycerol (v/v) with 20 µM taxol and 1 mM DTT) and resuspended as previously described[25] was incubated with motor solution in the dark for 15 min at RT. The Motor-microtubule mixture was laid on top of a glycerol centrifuged in a TLA120.2 rotor at 278,835 × g for 12 min at RT. Final pellet (Kinesin-bound microtubules) was washed with BRB80 (80 mM PIPES, 2 mM $MgCl_2$, and 1 mM EGTA, pH 7.0) and incubated in 100 µL of release buffer (80 mM PIPES, 2 mM $MgCl_2$, 1 mM EGTA, and 300 mM KCl, pH ~7 with 5mM Mg-ATP) for 5 min at RT. The supernatant was supplied with 660 mM sucrose and flash frozen. A typical kinesin prep yielded ~0.5 to 1 µM K560-GFP dimer.

Human dynactin was purified from stable cell lines expressing p62-Halo-3xFlag as described previously[65,66]. Briefly, cells were collected from 160 × 15 cm plates and resuspended in 80 mL of dynactin-lysis buffer (30 mM HEPES [pH 7.4], 50 mM potassium acetate, 2 mM magnesium acetate, 1 mM EGTA, 1 mM DTT, 10% (v/v) glycerol) supplemented with 0.5 mM Mg-ATP, 0.2% Triton X-100 and 1 cOmplete EDTA-free protease inhibitor cocktail tablet (Roche) per 50 mL and rotated slowly for 15 min. The lysate was clarified by centrifuging at 66,000 × g for 30 min in Type 70 Ti rotor (Beckman). The clarified supernatant was incubated with 1.5 mL of anti-Flag M2 affinity gel (Sigma-Aldrich) overnight on a roller. The beads were transferred to a gravity flow column, washed with 50 mL of wash buffer (dynactin-lysis buffer supplemented with 0.1 mM Mg-ATP, 0.5 mM Pefabloc and 0.02% Triton X-100), 100 mL of wash buffer supplemented with 250 mM potassium acetate, and again with 100 mL of wash buffer. Dynactin was eluted from beads with 1 mL of elution buffer (wash buffer with 2 mg/mL of 3xFlag peptide). The eluate was collected, filtered by centrifuging with Ultrafree-MC VV filter (EMD Millipore) in a tabletop centrifuge and diluted to 2 mL in Buffer A (50 mM Tris-HCl [pH 8.0], 2 mM MgOAc, 1 mM EGTA, and 1 mM DTT) and injected onto a MonoQ 5/50 GL column (GE Healthcare and Life Sciences) at 1 mL/min. The column was pre-washed with 10 column volumes (CV) of Buffer A, 10 CV of Buffer B (50 mM Tris-HCl [pH 8.0], 2 mM MgOAc, 1 mM EGTA, 1 mM DTT, 1 M KOAc) and again with 10 CV of Buffer A at 1 mL/min. To elute, a linear gradient was run over 26 CV from 35–100% Buffer B. Pure dynactin complex eluted from ~75–80% Buffer B. Peak fractions containing pure dynactin complex were pooled, buffer exchanged into a GF150 buffer supplemented with 10% glycerol, concentrated to 0.02-0.1 mg/mL using a 100K MWCO concentrator (EMD Millipore) and flash frozen in liquid nitrogen. Typical dynactin prep yields are between 150-300 nM.

Human dynein was purified from stable cells lines expressing an IC2-SNAPf-3xFlag as described previously[25]. Frozen pellets collected from ~60-100 × 15 cm plates were resuspended in dynein lysis buffer (25 mM HEPES pH 7.4, 50 mM KOAc, 2 mM MgOAc,1 mM EGTA, 10% glycerol (v/v), and 1 mM DTT) supplemented with 0.2% Triton X-100, 0.5 mM Mg-ATP, and cOmplete EDTA-free protease inhibitor cocktail. The lysate was centrifuged at 66,000 × g in a Ti-70 rotor for 30 min. The clarified supernatant was incubated with 1 mL of anti-Flag M2 affinity gel (Sigma-Aldrich) overnight on a roller. Beads were collected by gravity flow and washed with 50 mL wash buffer (dynein lysis buffer with 0.02% Triton X-100 and 0.5 mM Mg-ATP) supplemented with protease inhibitors (cOmplete Protease Inhibitor Cocktail, Roche). Beads were then washed with 50 mL high salt wash buffer (25 mM HEPES, pH 7.4, 300 mM KOAc, 2 mM MgOAc, 10% glycerol, 1 mM DTT, 0.02% Triton X-100, 0.5 mM Mg-ATP), and then with 100 mL wash buffer. For labelling, beads were resuspended in 1 mL wash buffer and incubated with 5 µM SNAP-Cell TMR Star (New England BioLabs) for 10 min on the column at RT. Unbound dye was removed with 100 mL wash buffer at 4 °C. Dynein was eluted with 1 mL of elution buffer (wash buffer containing 2 mg/mL 3xFLAG peptide). The eluate was collected, diluted to 2 mL in Buffer A (50 mM Tris pH 8.0, 2 mM MgOAc, 1 mM EGTA, and 1 mM DTT) and injected onto a MonoQ 5/50 GL column (GE Healthcare Life Sciences) at 0.5 mL/min. The column was washed with 20 CV of Buffer A at 1 mL/min. To elute, a linear gradient was run over 40 CV into Buffer B (50 mM Tris pH 8.0, 2 mM MgOAc, 1 mM EGTA, 1 mM DTT, 1 M KOAc). Pure dynein complex elutes from ~60–70% Buffer B. Peak fractions were pooled and concentrated, 0.1 mM Mg-ATP and 10% glycerol were added and the samples were snap frozen in liquid nitrogen. A typical preparation yielded 150-300 nM dynein.

Human NINL was purified as previously described[65]. pET28a-ZZ-TEV-Halo-NINL$^{1-702}$ was transformed into BL-21[DE3] cells (New England Biolabs) until OD 0.4-0.6 and expression was induced with 0.1 mM IPTG for 16 h at 18 °C. Frozen cell pellets from 1 L culture were resuspended in 40 mL of activator-lysis buffer (30 mM HEPES

[pH 7.4], 50 mM potassium acetate, 2 mM magnesium acetate, 1 mM EGTA, 1 mM DTT, 0.5 mM Pefabloc, 10% (v/v) glycerol) supplemented with 1 cOmplete EDTA-free protease inhibitor cocktail tablet (Roche) per 50 mL and 1 mg/mL lysozyme. The resuspension was incubated on ice for 30 min and lysed by sonication. The lysate was clarified by centrifuging at 66,000 × g for 30 min in Type 70 Ti rotor (Beckman). The clarified supernatant was incubated with 2 mL of packed IgG Sepharose 6 Fast Flow beads (GE Healthcare Life Sciences) for 2 h on a roller. The beads were transferred to a gravity flow column, washed with 100 mL of activator-lysis buffer supplemented with 150 mM potassium acetate and 50 mL of cleavage buffer (50 mM Tris–HCl [pH 8.0], 150 mM potassium acetate, 2 mM magnesium acetate, 1 mM EGTA, 1 mM DTT, 0.5 mM Pefabloc, 10% (v/v) glycerol). The beads were then resuspended and incubated in 15 mL of cleavage buffer supplemented with 0.2 mg/mL TEV protease overnight on a roller. The supernatant containing cleaved proteins were concentrated using a 50K MWCO concentrator (EMD Millipore) to 1 mL, filtered by centrifuging with Ultrafree-MC VV filter (EMD Millipore) in a tabletop centrifuge, diluted to 2 mL in Buffer A (30 mM HEPES [pH 7.4], 50 mM potassium acetate, 2 mM magnesium acetate, 1 mM EGTA, 10% (v/v) glycerol and 1 mM DTT) and injected onto a MonoQ 5/50 GL column (GE Healthcare and Life Sciences) at 0.5 mL/min. The column was pre-washed with 10 CV of Buffer A, 10 CV of Buffer B (30 mM HEPES [pH 7.4], 1 M potassium acetate, 2 mM magnesium acetate, 1 mM EGTA, 10% (v/v) glycerol and 1 mM DTT) and again with 10 CV of Buffer A at 1 mL/min. To elute, a linear gradient was run over 26 CV from 0–100% Buffer B. The peak fractions containing unlabelled Halo-tagged NINL were collected and concentrated to using a 50K MWCO concentrator (EMD Millipore) to 0.2 mL. A typical NINL prep yield was ~5-10 μM dimer.

Single-molecule microscopy and motility assays

Single-molecule imaging was performed using total internal reflection fluorescence (TIRF) microscopy with an inverted microscope (Nikon, Ti-E Eclipse) equipped with a 100x 1.49 N.A. oil immersion objective (Nikon, Plano Apo), and a MLC400B laser launch (Agilent), with 405 nm, 488 nm, 561 nm and 640 nm laser lines. Excitation and emission paths were filtered using single bandpass filter cubes (Chroma), and emitted signals were detected with an electron multiplying CCD camera (Andor Technology, iXon Ultra 888). Illumination and image acquisition were controlled with NIS Elements Advanced Research software (Nikon), and the xy position of the stage was controlled with a ProScan linear motor stage controller (Prior).

Single-molecule motility were performed in flow chambers as previously described[25] using the setup shown in the schematic in Fig. 4A. Biotin-PEG-functionalized coverslips (Microsurfaces) were adhered to a Superfrost Plus Microscope slide (ThermoFisher) using double-sided scotch tape. Each slide contained four flow-chambers. Taxol-stabilized microtubules (~15mg/mL) with ~10% biotin-tubulin and ~10% Alex405-tubulin were prepared as described previously[25]. For each motility experiment, 1 mg/mL Strepdavidin (in 30 mM HEPES, 2 mM MgOAc, 1mM EGTA, 10% glycerol) was incubated in the flow chamber for 3 min. A 1:150 dilution of taxol-stabilized microtubules in motility assay buffer (30 mM HEPES, 50 mM KOAc, 2 mM MgOAc, 1mM EGTA, 10% glycerol, 1 mM DTT, and 20 μM Taxol, pH 7.4) was added to the flow chamber for 3 min to adhere polymerized microtubules to the coverslip. Flow chambers containing adhered microtubules were washed twice with LRRK2 buffer (20 mM HEPES pH 7.4, 80 mM NaCl, 0.5 mM TCEP, 5% glycerol, 2.5 mM $MgCl_2$, 20 μM GDP). Flow chambers were then incubated for 5 min either with (1) LRRK2 buffer alone or with the indicated kinase inhibitors ("0 nM" $LRRK2^{RCKW}$ condition) or (2) LRRK2 buffer containing $LRRK2^{RCKW}$ either alone, with DMSO, or with kinase inhibitors. DMSO or drugs were incubated with LRRK2 buffer (± $LRRK2^{RCKW}$) for 10 min at RT before adding to the flow chambers. Prior to the addition of dynein and kinesin motors, the flow chambers were washed twice with motility assay buffer containing 1mg/mL casein. To assemble dynein-dynactin-ninein-like (NINL) complexes, purified dynein (10-15 nM), dynactin and NINL were mixed at 1:2:10 molar ratio and incubated on ice for 10 min. The final imaging buffer for motors contained motility assay buffer supplemented with an oxygen scavenger system, 71.5 mM β-mercaptoethanol and either 1 mM ATP (kinesin) or 2.5 mM ATP (dynein). The final concentrations of kinesin and dynein in the flow chambers were ~2.5 nM and ~0.3 nM, respectively. K560-GFP was imaged every 500 msecs for 2 min with 25% laser (488) power at 150 ms exposure time. Dynein-TMR-dynactin-NINL was imaged every 300 msec for 3 min with 25% laser (561) power at 100 msec. Each sample was imaged no longer than 15 min. Each technical replicate consisted of movies from at least two fields of view containing between 5 and 10 microtubules each.

Single-molecule motility assay analysis

Kymographs were generated from motility movies and quantified for run lengths, percent motility, and velocity using ImageJ (NIH). Specifically, maximum-intensity projections were generated from time-lapse sequences to define the trajectory of particles on a single microtubule. The segmented line tool was used to trace the trajectories and map them onto the original video sequence, which was subsequently re-sliced to generate a kymograph. Motile and immotile events (>1 s) were manually traced. Bright aggregates, which were less than 5% of the population, were excluded from the analysis. For dynein-dynactin-NINL, both stationary and diffusive events were grouped as immotile. Run length measurements were calculated from motile events only. Error bars for run length analysis were generated using a bootstrapping method (run length values from each condition were resampled 200x using an XLSTAT program for Excel) and statistical significance was established using a one-way ANOVA with Dunnett's test for multiple comparisons or an unpaired Welch's *t*-test for only one comparison. For percent motility per microtubule measurements, motile events (>1 s and >1μm) were divided by total events per kymograph. Velocity measurements were calculated from the inverse slopes of the motile event traces (>1 s and >1μm) only. Statistical analyses were performed in Prism8 (Graphpad).

Western blot analysis

293T cells were maintained in Dulbecco's modified Eagle's medium (containing 10% fetal bovine serum and 1% penicillin/streptomycin). For western blot quantification of LRRK2 protein expression (Extended Data Fig. 9l), cells were plated on 6-well dishes (150K cells per well) 24 h before transfection. Cells were transfected with 1 μg of GFP-I2020T using polyethylenimine (PEI, Polysciences). After 48 h, cells were treated for 30 min with either 5 μM GZD-824 or DMSO-matched control. Cells were lysed on ice in RIPA buffer (50 mM Tris pH 7.5, 150 mM NaCl, 0.2% TritonX-10, 0.1%SDS, 0.5% Na-Deoxycholate, with cOmplete protease inhibitor cocktail). Lysates were further rotated for 15 min at 4 °C and clarified by centrifuging at 13,000 × g for 15 min. Clarified supernatants were boiled for 5 min in Laemmli buffer. The experiments were performed in triplicate.

For western blots, lysates were run on 4–12% gradient SDS–PAGE (Life Technologies) for 60 min and transferred to nitrocellulose for 3 h at 250 mA. Blots were dried at RT for 30 min, rinsed in 1x Tris buffered saline (TBS), followed by blocking with 5% milk in TBS. Antibodies were diluted in 5% milk in TBS-0.1% Tween-20 (TBS-T). Primary antibodies were incubated overnight at 4°C and Infrared (IR) secondary antibodies were incubated at RT for 45 min. For quantification of LRRK2 expression levels, blots were imaged on an Odyssey CLx controlled by Imaging Studio software (v5.2). DMSO and GZD-824 conditions were quantified in triplicate and normalized to a GAPDH loading control using Empiria Studio software (Li-COR). To ensure quantification was in the combined linear range for antibodies detecting both GFP-LRRK2 and GAPDH, a linear dilution series of lysates from cells expressing GFP-LRRK2 was also quantified by IR western blot.

Immunofluorescence, confocal microscopy and image analysis

The day before transfection, 293T cells were plated on acid-treated coverslips (Bellco Glass) pre-coated with 100 µg/mL Poly-D-lysine (Sigma) and 4 µg/mL Mouse Laminin (ThermoFisher) in 24-well plates (35K cells per well). Cells were transfected with 500 ng plasmid of either pDEST53-GFP-LRRK2 or pDEST53-GFP-LRRK2(I2020T) using PEI. After 48-72 h, cells were incubated with either a kinase inhibitor or DMSO-matched control (matched for time and concentration). For the Type I inhibitor experiment, cells were incubated with DMSO or Mli-2 (500 nM) for 2 h. For the Type II inhibitor, cells were incubated with DMSO or GZD-824 (5 or 10 µM) for 30 min. Cells were quickly washed 1x on ice with ice-cold PBS, and fixed with ice-cold 4% PFA/90% Methanol/5mM sodium bicarbonate for 10 min at -20 °C. Following fixation, the wells were immediately washed 3x with ice-cold PBS. Blocking buffer (1% BSA, 5% normal goat serum, 0.3%TritonX-100 in PBS) was added for 1 h at RT. Primary antibodies were diluted (1:500) in antibody dilution buffer (1% BSA, 0.1% TritonX-100 in PBS) and incubated overnight at 4 °C. After overnight incubation, the wells were washed 3x in PBS and incubated with secondary antibodies (1:500) in antibody dilution buffer for 1 h at RT. After secondary incubation, the wells were washed 3x in PBS, 1x in ddH2O and mounted using CitiFluor AF2 (EMS) on Superfrost Plus Microscope slides (ThermoFisher). Coverslips were sealed with nail polish and stored at 4 °C.

For the LRRK2 filament analysis in Fig. 5, experimenters were blinded to condition for both the imaging acquisition and analysis. Cells were imaged using a Nikon A1R HD confocal microscope with a LUN-V laser engine (405nm, 488nm, 561nm, and 640nm) and DU4 detector using bandpass and longpass filters for each channel (450/50, 525/50, 595/50, and 700/75). Slides were imaged on a Nikon Ti2 body using an Apo 60x 1.49 NA objective. Image stacks were acquired in resonant scanning mode with bidirectional scanning and 4x line averaging and 1.2 airy units. The lasers used were 405 nm, 488 nm and 561 nm. Illumination and image acquisition were controlled by NIS Elements Advanced Research software (Nikon Instruments). ImageJ was used to quantify the percent of cells with LRRK2 filaments. Maximum-intensity projections were generated from *z*-stack confocal images. Using the GFP immunofluorescence signal, transfected cells were traced. Cells were scored for the presence or absence of filaments using both the z-projection and z-stack micrographs as a guide. The presence of filaments was scored if the cells had either (a) a GFP filament signal greater than 5 µm or (b) bundles of filaments with at least two identifiable crosses. To calculate the percent cells with filaments, the number of cells with filaments was divided by the total number of transfected cells per technical replicate (defined as one 24-well coverslip). Approximately 20 cells were quantified per replicate for each condition in Fig. 5D (DMSO v. Mli-2) and between 40-100 cells were quantified per replicate for each condition in Fig. 5F (DMSO v. GZD-824). The quantification of all cellular experiments comes from data collected on three separate days except for the 10 µM GZD-824 condition in Fig. 5F which was performed on two separate days. All statistical analyses were performed in Prism8 (Graphpad).

Reporting summary

Further information on research design is available in the Nature Research Reporting Summary linked to this paper.

Data availability

All reagents and data will be made available upon request. Model coordinates for the LRRK2^{RCKW} structure are deposited in the Protein Data Bank (PDB) as follows: (1) PDB accession code 6VP6: LRRK2^{RCKW} with the adjacent COR-B and WD40 domains (from the trimer) used to optimize residues at those interfaces during refinement in Rosetta, with GDP-Mg^{2+} bound; (2) PDB accession code 6VNO: The top 10 models for LRRK2^{RCKW} without adjacent domains, with GDP-Mg^{2+} bound; (3) PDB accession code 6VP8: LRRK2^{RCKW} with the adjacent COR-B and WD40 domains (from the trimer) used to optimize residues at those interfaces during refinement in Rosetta, no GDP-Mg^{2+}; (4) PDB accession code 6VP7: The top 10 models for LRRK2^{RCKW} without adjacent domains, no GDP-Mg^{2+} bound. Cryo-EM maps for the different LRRK2^{RCKW} structures are deposited at the EMDB as follows: (1) EMD accession code 21250: This deposition contains both the 3.5Å map of LRRK2^{RCKW} trimer (used to build the COR-B, kinase and WD40 domains) and the 3.8Å map of the signal-subtracted LRRK2^{RCKW} trimer (used to build the RoC and COR-A domains); (2) EMD accession code 21306: 8.1Å map of LRRK2^{RCKW} monomer; (3) EMD accession code 21309: 9.5Å map of COR-mediated LRRK2^{RCKW} dimer in the absence of kinase ligand ("apo"); (4) EMD accession code 21310: 13.4Å map of WD40-mediated LRRK2^{RCKW} dimer in the absence of kinase ligand ("apo"); (5) EMD accession code 21311: 9.0Å map of COR-mediated LRRK2^{RCKW} dimer in the presence of MLi-2; (6) EMD accession code 21312: 10.2Å map of WD40-mediated LRRK2^{RCKW} dimer in the presence of MLi-2. Source data for EDF10 are provided with the paper. All other data that support the findings of this study are available from the corresponding authors upon reasonable request.

45. Pettersen, E. F. et al. UCSF Chimera–a visualization system for exploratory research and analysis. *J. Comput. Chem.* **25**, 1605–1612 (2004).
46. Charrier, J.-D. et al. Discovery and structure-activity relationship of 3-aminopyrid-2-ones as potent and selective interleukin-2 inducible T-cell kinase (Itk) inhibitors. *J. Med. Chem.* **54**, 2341–2350 (2011).
47. Woehlke, G. et al. Microtubule interaction site of the kinesin motor. *Cell* **90**, 207–216 (1997).
48. Suloway, C. et al. Automated molecular microscopy: the new Leginon system. *J. Struct. Biol.* **151**, 41–60 (2005).
49. Zheng, S. Q. et al. MotionCor2: anisotropic correction of beam-induced motion for improved cryo-electron microscopy. *Nat. Methods* **14**, 331–332 (2017).
50. Lander, G. C. et al. Appion: an integrated, database-driven pipeline to facilitate EM image processing. *J. Struct. Biol.* **166**, 95–102 (2009).
51. Roseman, A. M. FindEM-a fast, efficient program for automatic selection of particles from electron micrographs. *J. Struct. Biol.* **145**, 91–99 (2004).
52. Zivanov, J. et al. New tools for automated high-resolution cryo-EM structure determination in RELION-3. *eLife* **7**, (2018).
53. Punjani, A., Rubinstein, J. L., Fleet, D. J. & Brubaker, M. A. cryoSPARC: algorithms for rapid unsupervised cryo-EM structure determination. *Nat. Methods* **14**, 290–296 (2017).
54. Henderson, R. et al. Outcome of the first electron microscopy validation task force meeting. in *Structure (London, England : 1993)* 205–214 (MRC Laboratory of Molecular Biology, Hills Road, Cambridge CB2 0QH, UK., 2012).
55. Scheres, S. H. W. & Chen, S. Prevention of overfitting in cryo-EM structure determination. *Nat. Methods* **9**, 853–854 (2012).
56. Rosenthal, P. B. & Henderson, R. Optimal determination of particle orientation, absolute hand, and contrast loss in single-particle electron cryomicroscopy. *J. Mol. Biol.* **333**, 721–745 (2003).
57. Chen, S. et al. High-resolution noise substitution to measure overfitting and validate resolution in 3D structure determination by single particle electron cryomicroscopy. *Ultramicroscopy* **135**, 24–35 (2013).
58. Wang, R. Y.-R. et al. Automated structure refinement of macromolecular assemblies from cryo-EM maps using Rosetta. *eLife* **5**, 352 (2016).
59. Emsley, P. & Cowtan, K. Coot: model-building tools for molecular graphics. *Acta Crystallogr. D Biol. Crystallogr.* **60**, 2126–2132 (2004).
60. Söding, J., Biegert, A. & Lupas, A. N. The HHpred interactive server for protein homology detection and structure prediction. *Nucleic Acids Res.* **33**, W244-8 (2005).)
61. Greggio, E. et al. The Parkinson's disease kinase LRRK2 autophosphorylates its GTPase domain at multiple sites. *Biochem. Biophys. Res. Commun.* **389**, 449–454 (2009).
62. Wagner, T. et al. Roderer, Daniel, Tacke, S., Siebolds, B., Schubert, E., Shaikh, T. R., Lill, P., Gatsogiannis, C. & Raunser, S. SPHIRE-crYOLO is a fast and accurate fully automated particle picker for cryo-EM. *Commun. Biol.* **2**, (2018).
63. Lis, P. et al. Development of phospho-specific Rab protein antibodies to monitor *in vivo* activity of the LRRK2 Parkinson's disease kinase. *Biochem. J.* **475**, 1–22 (2018).
64. Nicholas, M. P., Rao, L. & Gennerich, A. An improved optical tweezers assay for measuring the force generation of single kinesin molecules. *Methods Mol. Biol.* **1136**, 171–246 (2014).
65. Htet, Z. M. et al. LIS1 promotes the formation of activated cytoplasmic dynein-1 complexes. *Nat. Cell Biol.* **22**, 518–525 (2020).
66. Kendrick, A. A. et al. Hook3 is a scaffold for the opposite-polarity microtubule-based motors cytoplasmic dynein-1 and KIF1C. *J. Cell Biol.* **218**, 2982–3001 (2019).

Acknowledgements We thank Susan Taylor for her role in initiating this collaborative work, which was partially supported by multi-investigator grants from the Michael J Fox Foundation: grant #s: 11425 and 11425.02 (PI: Susan Taylor) and 18321 (PIs: AEL and SLR-P). We also thank the UC San Diego Cryo-EM Facility, the Nikon Imaging Center at UC San Diego, where the confocal microscopy was performed, the use of instruments at the Electron Imaging Center for NanoMachines supported by NIH (1S10RR23057, 1S10OD018111, and 1U24GM116792), NSF (DBI-1338135) and CNSI at UCLA, John P. Gillies and Agnieszka Kendrick for technical support with protein purifications, and Andrea Dickey for feedback on the manuscript. CKD was initially supported by the Molecular Biophysics Training Grant (NIH Grant T32 GM008326) and

subsequently by a Predoctoral Fellowship from the Visible Molecular Cell Consortium and Center for Trans-scale Structural Biology (UC San Diego). DS is supported by an A.P. Giannini Foundation postdoctoral fellowship. AKS receives salary and support from the Ludwig Institute for Cancer Research. EV is supported by a NIH Director's New Innovator Award DP2GM123494. SLR-P is an investigator of the Howard Hughes Medical institute and is also supported by R01GM121772. AEL is supported by R01GM107214. SK is grateful for support from the SGC, a registered charity that receives funds from AbbVie, Bayer Pharma AG, Boehringer Ingelheim, Canada Foundation for Innovation, Eshelman Institute for Innovation, Genome Canada, Innovative Medicines Initiative EUbOPEN (agreement No 875510), Janssen, Merck KGaA, MSD, Ontario Ministry of Economic Development and Innovation, Pfizer, São Paulo Research Foundation-FAPESP, Takeda, and the Wellcome, as well as Boehringer Ingelheim for funding initial structural studies of this project. Most of this work is described in the thesis by C.K.D. (https://escholarship.org/content/qt95k5q45v/qt95k5q45v.pdf?t=q87k6q).

Author contributions CKD collected and processed the cryo-EM data. JS performed the single-molecule and cellular assays with the help of OD. SM designed the LRRK2^{RCKW} construct and purified the protein. CKD and IL built the molecular model of LRRK2^{RCKW}. DS performed the SEC-MALS and phosphorylation assays. MM collected and analyzed the LRRK2^{RCKW} and microtubule cryo-EM data. RW and JB performed the cellular cryo-ET. AKS contributed to the structural analysis and provided advice on the selection of kinase inhibitors. SK, EV, SLR-P and AEL directed and supervised the research. CKD, JS, SLR-P and AEL wrote the manuscript and SM, DS, MM, OD, AKS, SK and EV edited it.

Competing interests The authors declare no competing interests.

Additional information

Supplementary information is available for this paper at https://doi.org/10.1038/s41586-020-2673-2.

Correspondence and requests for materials should be addressed to S.L.R.-P. or A.E.L.

Peer review information *Nature* thanks Asa Abelovich, Henning Stahlberg and the other, anonymous, reviewer(s) for their contribution to the peer review of this work.

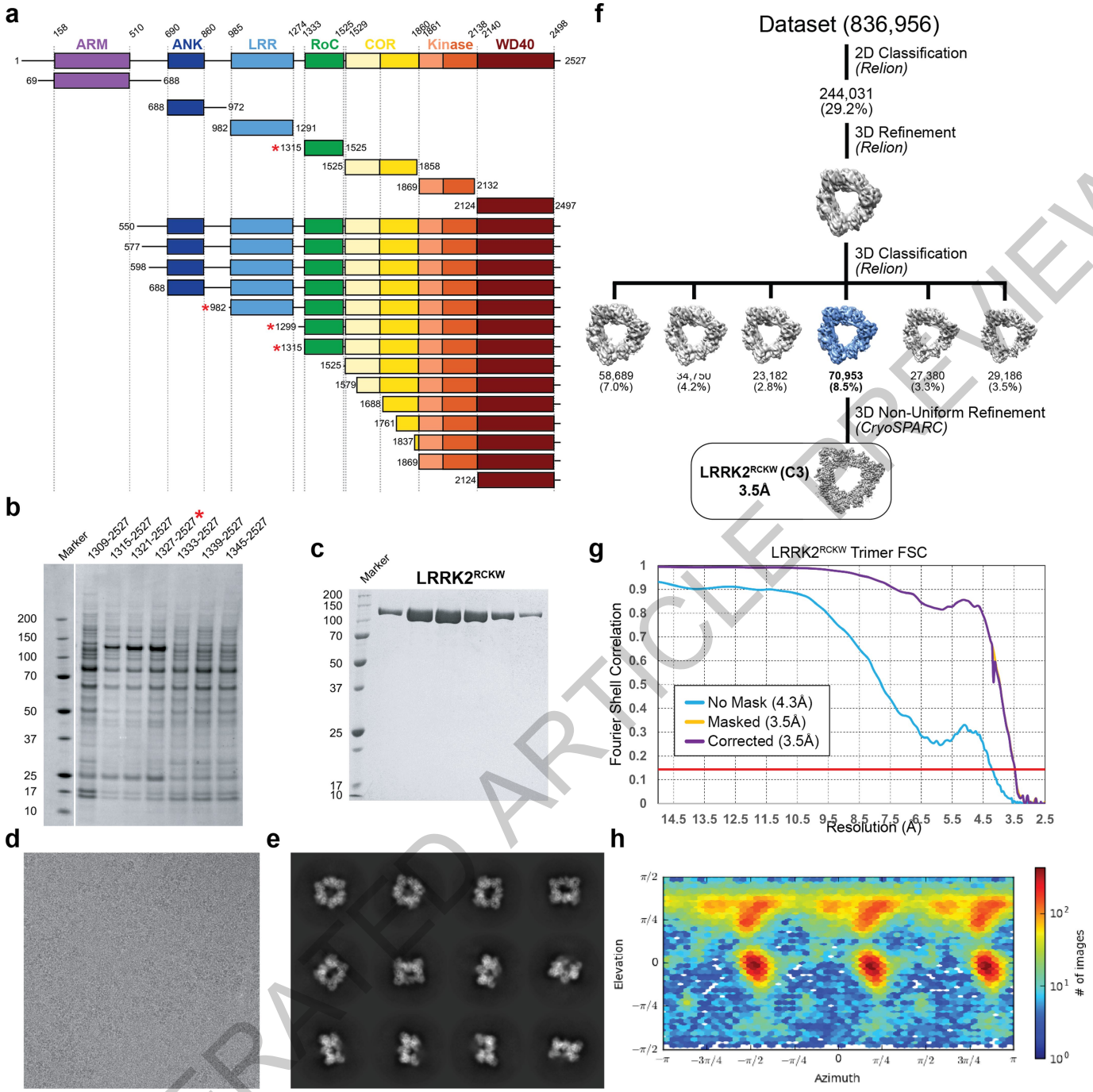

Extended Data Fig. 1 | Optimization of LRRK2 constructs and cryo-EM analysis of a LRRK2^{RCKW} trimer. a, We systematically scanned domain boundaries (amino acid numbers of boundaries noted above domain names) to generate LRRK2 constructs that expressed well in baculovirus-infected insect cells and yielded stable and soluble protein. These attempts included full-length LRRK2, the kinase domain alone or with the WD40 domain, and other isolated domains. In this approach, only the GTPase domain on its own expressed well. Next, we gradually shortened LRRK2 from its amino terminus. Red asterisks indicate constructs that were soluble. **b**, After identifying domain boundaries yielding constructs that expressed soluble protein, additional fine tuning of boundaries was performed. A Coomassie stained SDS–PAGE gel shows systematic N-terminal truncations at the RoC domain resulting in the identification of a construct with the highest expression levels: amino acids 1327 to 2527 (red asterisk, "LRRK2^{RCKW}" here). **c**, A Coomassie stained SDS–PAGE gel of purified LRRK2^{RCKW} after elution from an S200 gel filtration column. As predicted by its primary structure, LRRK2^{RCKW} runs at ~140 kDa. **d**, Electron micrograph of LRRK2^{RCKW}. **e**, 2D class averages of the LRRK2^{RCKW} trimer. **f**, 2D/3D classification scheme used to obtain the 3.5Å structure of the LRRK2^{RCKW} trimer. **g, h**, Fourier Shell Correlations (from Cryosparc) (d) and Euler angle distribution (e) for the LRRK2^{RCKW} trimer.

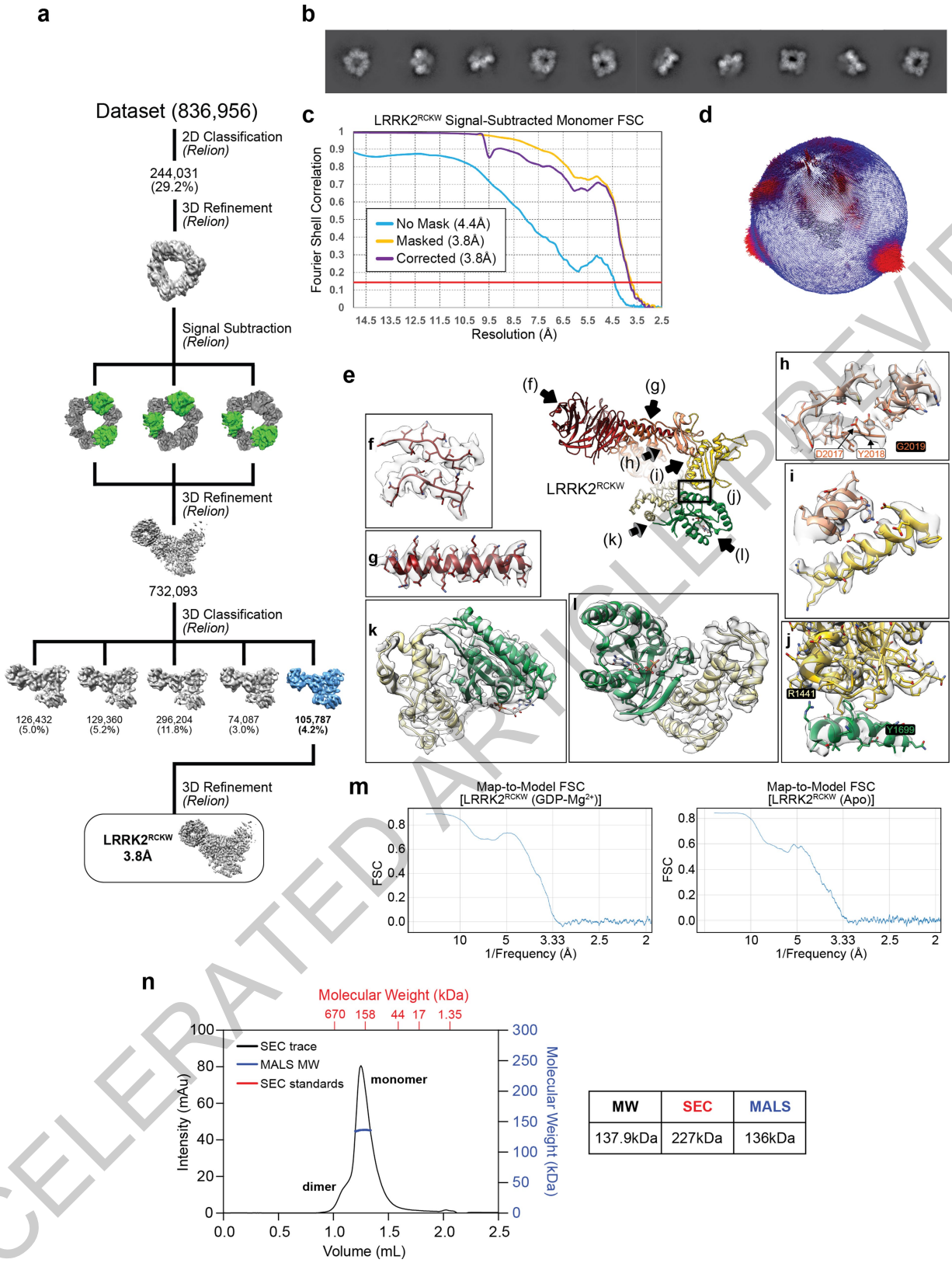

MW	SEC	MALS
137.9kDa	227kDa	136kDa

Extended Data Fig. 2 | See next page for caption.

Extended Data Fig. 2 | Cryo-EM analysis of a signal-subtracted LRRK2^{RCKW} trimer and map-to-model fit. a, Processing strategy used to obtain a 3.8Å structure of LRRK2^{RCKW} generated from a signal-subtracted trimer where only one monomer contains the RoC and COR-A domains. This structure improved the resolution of the RoC and COR-A domains relative to the full trimer (Extended Data Fig. 1). **b-d**, 2D class averages (b), Fourier Shell Correlations (from Relion) (c), and Euler angle distribution (from Relion) (d) for the 3.8Å-resolution signal-subtracted LRRK2^{RCKW} structure. **e**, Close-ups (f-l) of different parts of the final model fit into the map. **f**, Section of the WD40 domain. **g**, C-terminal helix and its interface with the kinase domain. **h**, Active site of the kinase. Residues in the DYG motif are labelled. G2019, the site of a major PD-associated mutation (G2019S) and the last residue of the activation loop seen in our structure, is highlighted by a black rounded square. **i**, Interface between COR-B and the αC helix of the N-lobe of the kinase domain. **j**, Interface between the RoC and COR-B domains. R1441 and Y1699, two residues mutated in PD, are labelled. **k**, **l**, Two different views of the RoC and COR-A domains with GDP-Mg^{2+} modelled into the density. Side chains were omitted in these two panels, corresponding to the lowest-resolution parts of the map. **m**, Map-to-model FSC plots for the top-ranked LRRK2^{RCKW} models, with (left) or without GDP-Mg2+ (right) in the RoC domain. The 0.143 FSC values are reported in Supplementary Table 1. **n**, Size Exclusion Chromatography-Multiple Angle Light Scattering (SEC-MALS) analysis of LRRK2^{RCKW} under the conditions used for cryo-EM (Fig. 1). The table shows the calculated molecular weights (MW) of LRRK2^{RCKW} according to SEC standards ("SEC") and MALS.

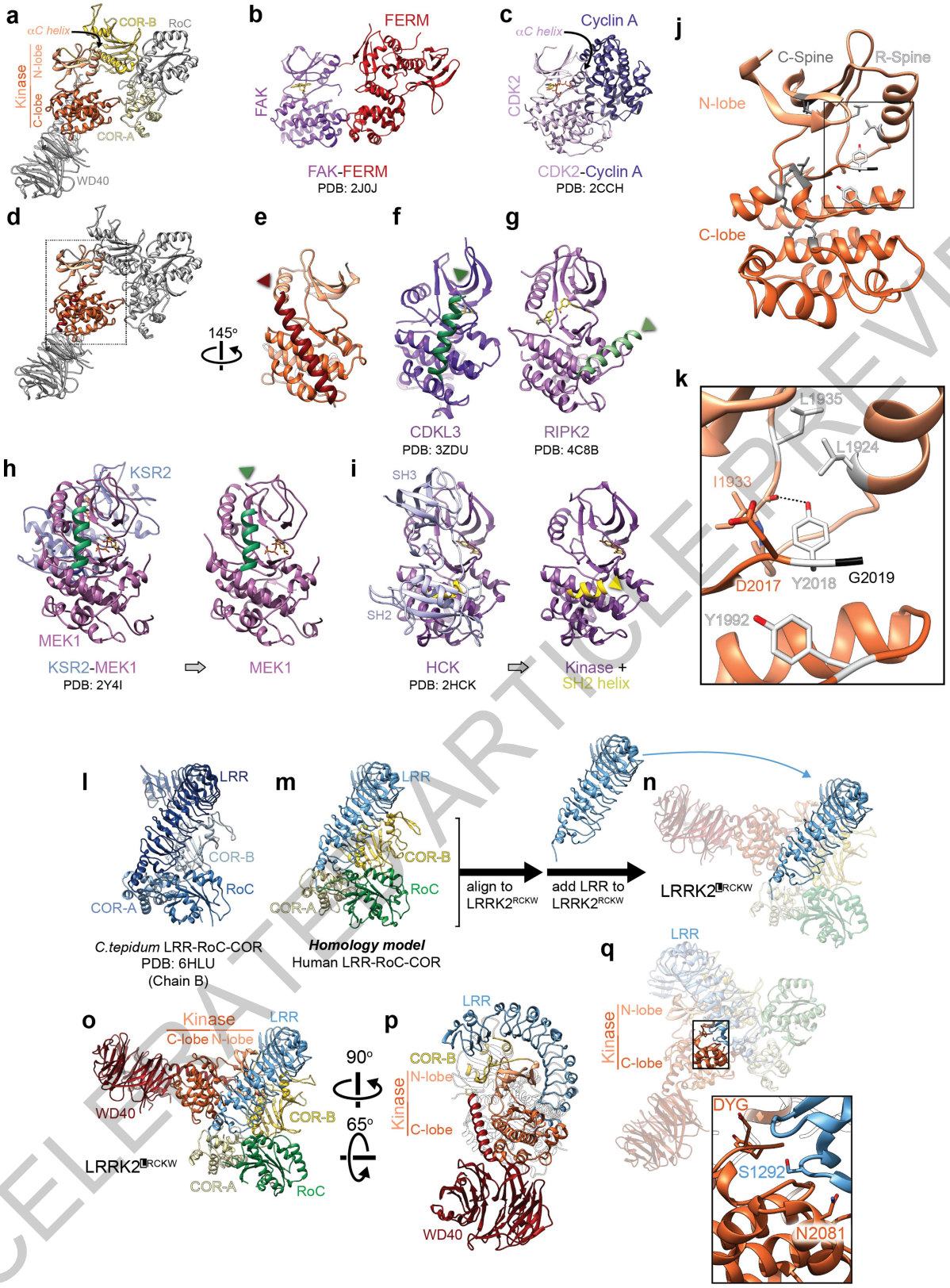

Extended Data Fig. 3 | See next page for caption.

Extended Data Fig. 3 | Comparisons between LRRK2 and other kinases and modelling of the Leucine-Rich Repeat (LRR) into LRRK2^{RCKW}. **a**, View of the LRRK2^{RCKW} atomic model with COR-A, COR-B and kinase domains colored. The N- and C-lobes of the kinase are labelled, as is the αC helix in the N-lobe. **b, c**, The FAK-FERM (PDB: 2J0J)[17] (b) and CDK2-Cyclin A (PDB: 2CCH)[19] (c) complexes, shown in the same orientation as the kinase in (a). The αC helix of CDK2 is also labelled. **d**, Same view as in (a) with only the kinase domain and the C-terminal helix colored. **e**, Rotated view of LRRK2's kinase domain with the C-terminal helix facing the viewer. **f, g**, CDKL3 (PDB: 3ZDU) (f) and RIPK2 (PDB: 4C8B)[32] (g) shown in the same orientation as LRRK2's kinase in (e), with alpha helices with the same general location as LRRK2's C-terminal helix colored in green. **h**, KSR2-MEK1 complex (PDB: 2Y4I), with the kinase oriented as in (e) (left) and after removing KSR2 for clarity (right). The alpha helix associated with the kinase is shown in green. **i**, HCK (PDB: 2HCK) in complex with its SH2 and SH3 domains with the kinase oriented as in (e) (left), and after removal of the SH2 and SH3 domains for clarity (right). A remaining alpha helix from the SH2 domain is shown in yellow. **j**, Front view of LRRK2's kinase with the C-Spine and R-Spine residues colored in grey and white, respectively. **k**, Close-up of the DYG motif and neighbouring R-Spine residues. A putative hydrogen bond between Y2018 and the backbone carbonyl of I1933 is shown (O-O distance: 2.7Å). This interaction provides a structural explanation for the hyperactivation of the kinase resulting from a Y2018F mutation[38], which would release the activation loop. **l**, Crystal structure of the LRR-RoC-COR(A/B) domains from *C. tepidum* Roco (PDB: 6HLU)[7]. **m**, Homology model for human LRR-RoC-COR(A/B) based on the *C. tepidum* Roco structure (from SWISS-MODEL). **n**, Chimeric model combining LRRK2^{RCKW} and the homology model for the LRR domain from (m) obtained by aligning their RoC-COR(A/B) domains. **o**, **p**, Two views of the hybrid LRRK2^{LRCKW} model. **q**, Close-up showing the proximity between the active site of the kinase (with the side chains of its DYG motif shown) and the S1292 autophosphorylation site on the LRR. The close-up also highlights the proximity between N2081, a residue implicated in Crohn's Disease, and the LRR.

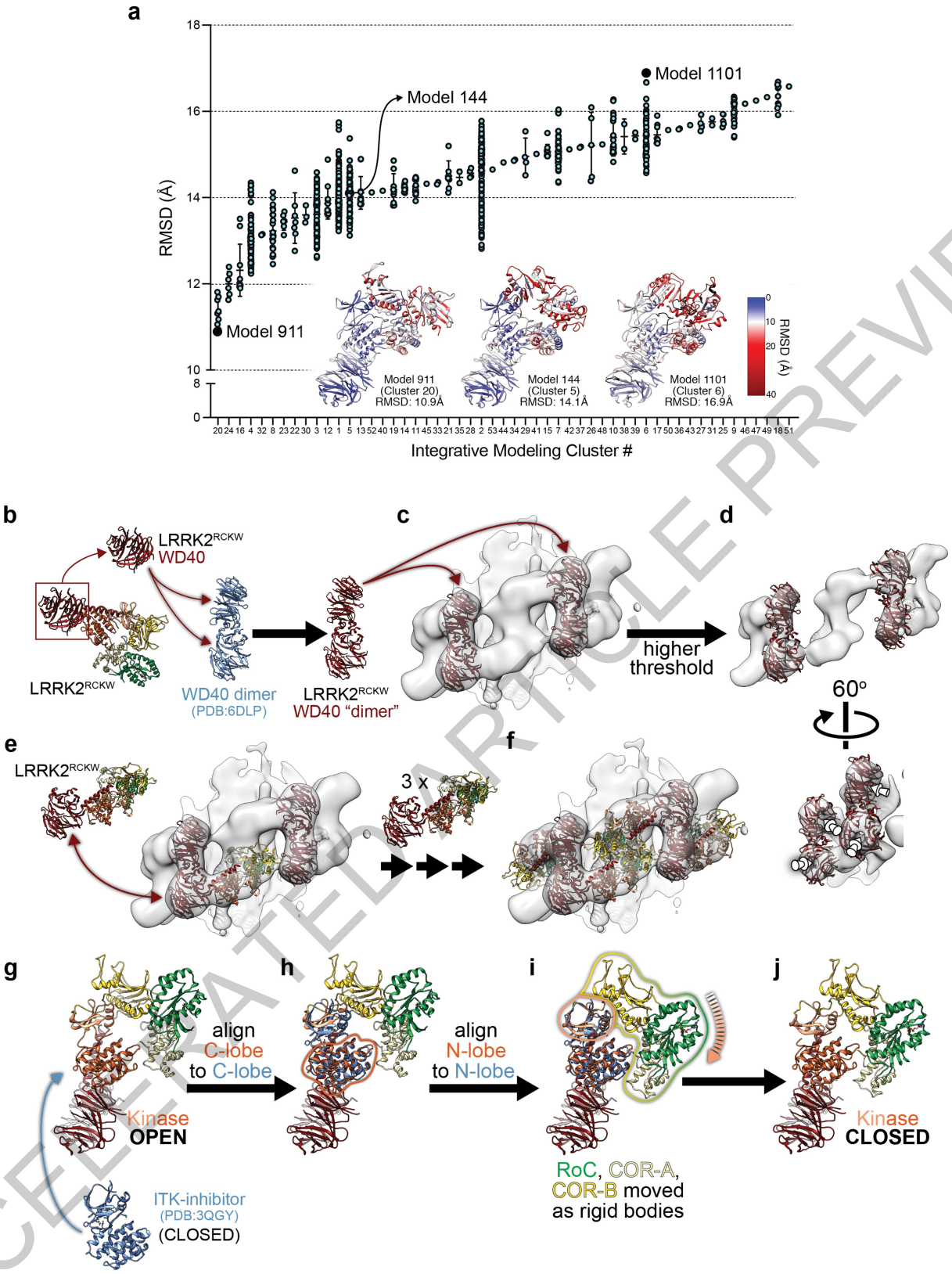

Extended Data Fig. 4 | See next page for caption.

Extended Data Fig. 4 | Comparison between LRRK2^{RCKW} and integrative models built into cryo-ET maps of LRRK2 filaments in cells and docking of LRRK2^{RCKW} into those maps. a, Root-mean-square deviation (r.m.s.d.) between the atomic model of LRRK2^{RCKW} and each of the 1,167 integrative models generated by Watanabe, Buschauer, Bohning and colleagues[5]. RMSDs were calculated in Chimera[45] using 100% residue similarity and with pruning iterations turned off. r.m.s.d. values are grouped into 53 clusters of related models (see[5] for details), with the mean and standard deviation shown whenever the cluster contains two or more models. Integrative models that gave the lowest, median and highest r.m.s.d. values are shown. The models are colored according to the per-residue r.m.s.d. with the atomic model of LRRK2^{RCKW}. **b**, The WD40 s in the crystal structure of a dimer of LRRK2's WD40 (PDB: 6DLP)[9] were replaced with the WD40 s from our cryo-EM structure of LRRK2^{RCKW}. **c**, The resulting dimer was fitted into the 14Å cryo-ET map of cellular microtubule-associated LRRK2 filaments[5]. **d**, Two views of the same fitting shown in (c), displayed with a higher threshold for the map to highlight the fitting of the WD40 β-propellers into the density. The white arrows point towards the holes at the centre of the β-propellers densities. **e**, Four copies of LRRK2^{RCKW} were docked into the cryo-ET map by aligning their WD40 domains to the docked WD40 dimer. **f**, Model containing the four aligned LRRK2^{RCKW}. **g-j**, Modelling of the kinase-closed form of LRRK2^{RCKW}. **g, h**, The structure of ITK bound to an inhibitor (PDB: 3QGY)[46], which is in a closed conformation, was aligned to LRRK2^{RCKW} using only the C-lobes of the two kinases. **i**, The N-terminal portion of LRRK2^{RCKW}, comprising RoC, COR-A, COR-B and the N-lobe of the kinase, was aligned to ITK using only the N-lobes of the kinases. RoC, COR-A and COR-B were moved as a rigid body in this alignment. **j**, Kinase-closed model of LRRK2^{RCKW}.

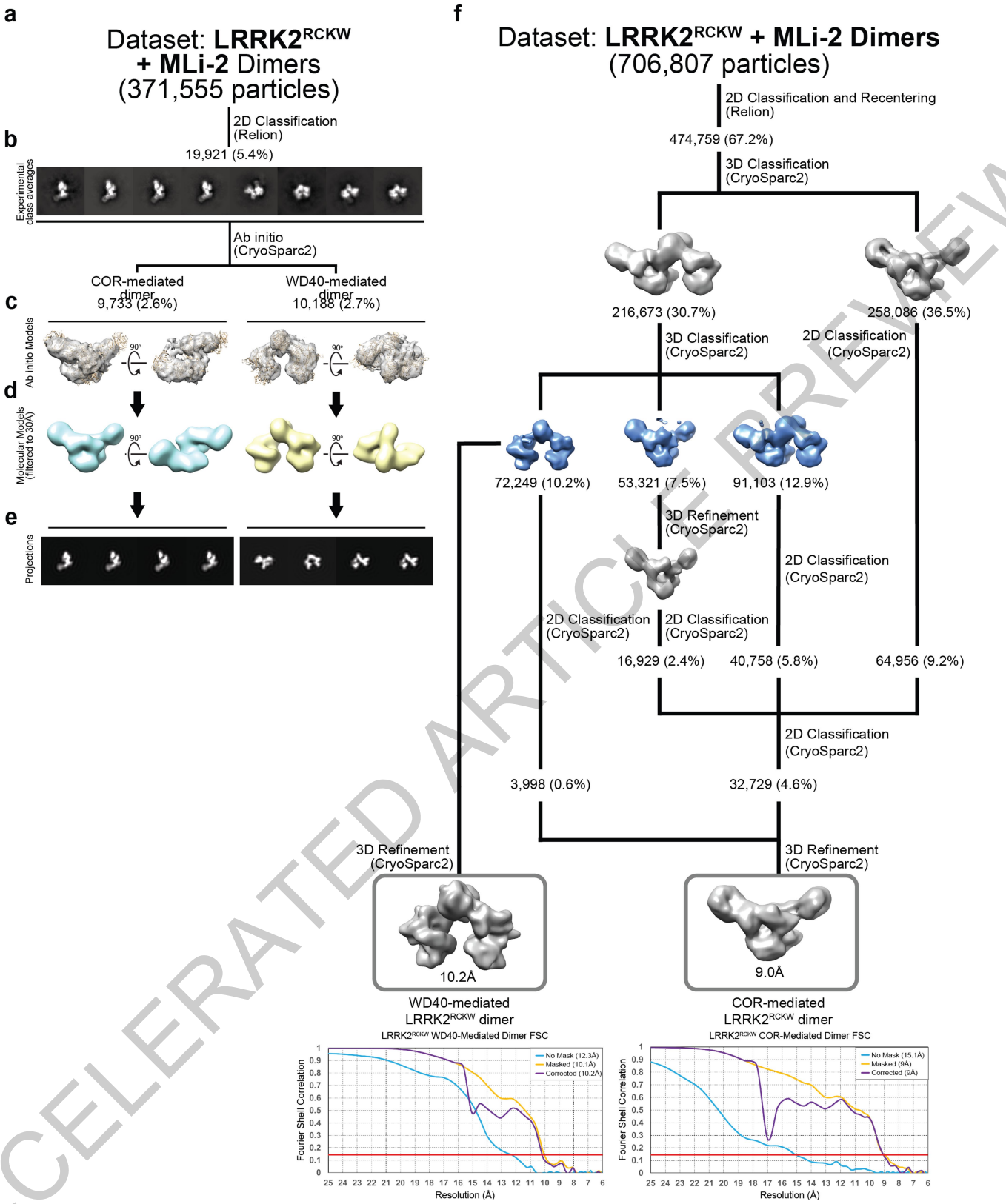

Extended Data Fig. 5 | Ab initio models for cryo-EM of LRRK2^{RCKW} dimers and cryo-EM analysis of WD40- and COR-mediated dimers of LRRK2^{RCKW} in the presence of the inhibitor MLi-2. a, An initial data set was collected from a sample of LRRK2^{RCKW} incubated in the presence of the kinase inhibitor MLi-2 and dimers were selected. **b**, Representative two-dimensional class averages used for ab initio model building. **c**, Ab initio models with the structure of LRRK2^{RCKW} docked in. **d**, Volumes generated form the molecular models in (b), filtered to 30Å resolution. **e**, Projections of the volumes in (d) shown in the same order as their corresponding 2D class averages in (b). **f**, Data processing strategy for obtaining cryo-EM structures of WD40- and COR-mediated dimers of LRRK2^{RCKW} in the presence of the inhibitor MLi-2. The models used during this processing (see Methods) are those shown in (d) along with an additional linear trimer (see Methods) used for particle sorting.

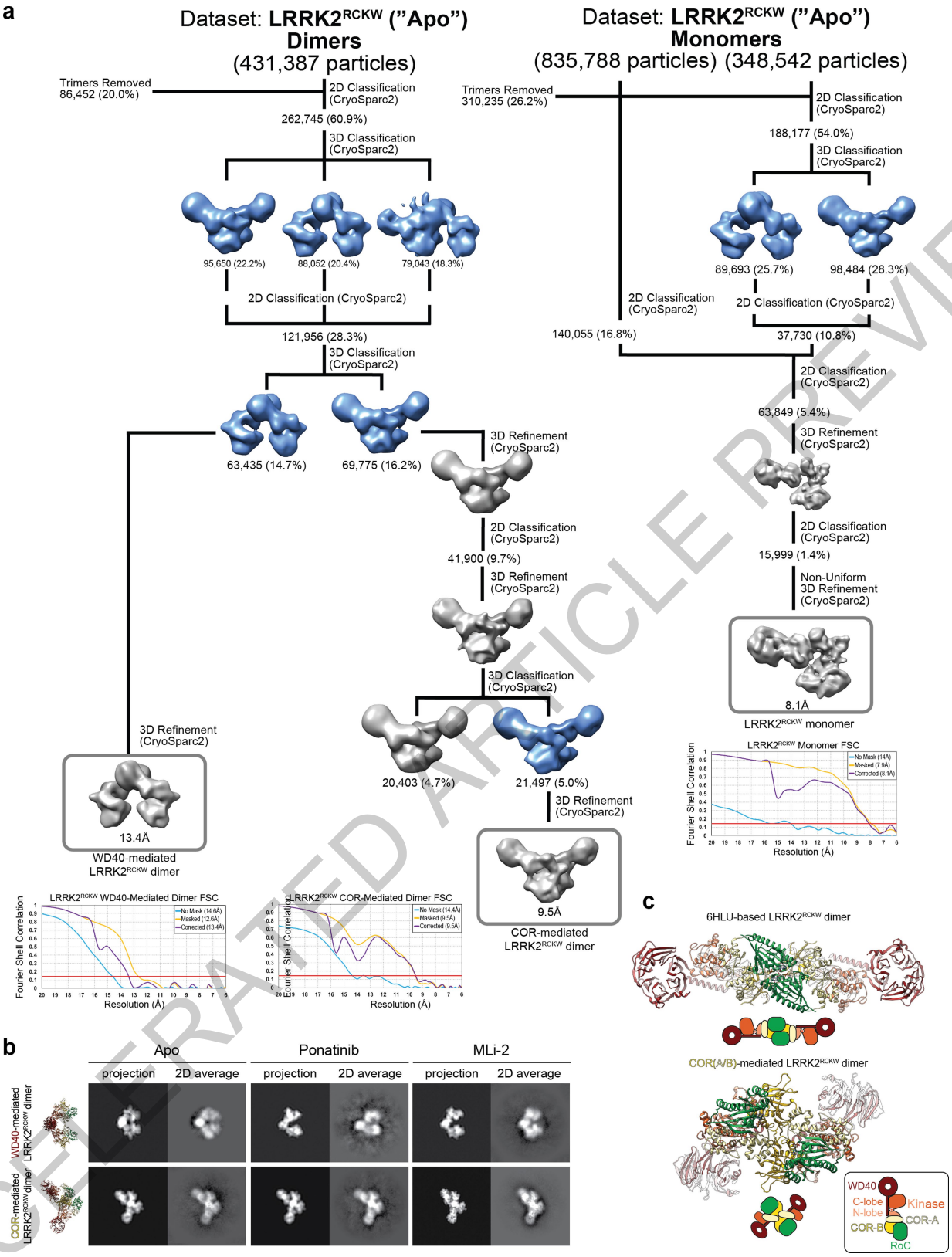

Extended Data Fig. 6 | See next page for caption.

Extended Data Fig. 6 | Cryo-EM analysis of a monomer and WD40- and COR-mediated dimers of LRRK2^{RCKW} in the absence of inhibitor ("Apo") and dimerization of LRRK2^{RCKW} outside the filaments. a, Data processing strategy for obtaining cryo-EM structures of a monomer and WD40- and COR-mediated dimers of LRRK2^{RCKW} in the absence of inhibitor. The models used during the processing of the dimers (see Methods) are those shown in Extended Data Fig. 5d, along with an additional linear trimer (see Methods) used for particle sorting. The models used for processing of the monomer (see Methods) were the same dimer models as in Extended Data Fig. 5d (used for particle sorting) in addition to a monomer model generated from our LRRK2^{RCKW} model (used for refinement). **b**, Two-dimensional (2D) class averages of WD40- and COR-mediated LRRK2^{RCKW} dimers obtained in the absence of inhibitors ("Apo") or in the presence of either Ponatinib or MLi-2. The same molecular models of the two dimers shown in Fig. 3 are shown on the left but in orientations similar to those represented by the 2D class averages shown here. For each class average, a projection from the corresponding model in the best-matching orientation is shown to its left. **c**, Two copies of the LRRK2^{RCKW} structure were aligned to the RoC-COR domains of the LRR-RoC-COR structure from *C. tepidum*'s Roco protein (PDB: 6HLU) to replicate the interface observed in the bacterial homologue in the context of the human protein. This panel shows a comparison between the dimer modelled based on the *C. tepidum* LRR-RoC-COR structure and the dimer observed for LRRK2^{RCKW} in this work. While the bacterial structure shows a dimerization interface that involves the GTPase (RoC), LRRK2^{RCKW} interacts exclusively through its COR-A and -B domains, with the RoC domains located away from this interface. The two arrangements are shown schematically in cartoon form below the structures.

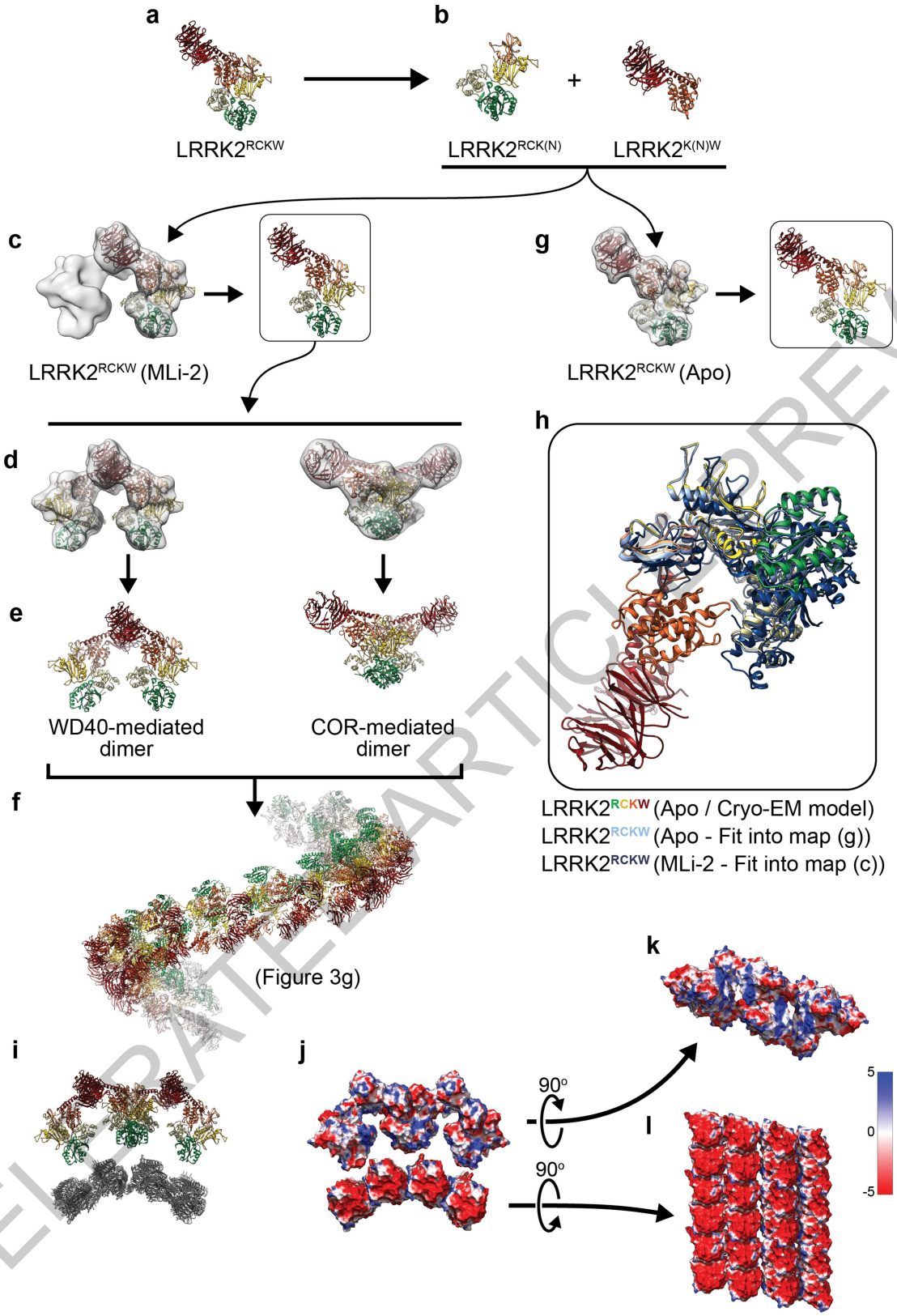

Extended Data Fig. 7 | See next page for caption.

Extended Data Fig. 7 | Properties of the microtubule-associated LRRK2^{RCKW} filaments. a, b, The LRRK2^{RCKW} structure solved in this work (a) was split at the junction between the N- and C-lobes of the kinase domain (L1949-A1950) (b). **c**, Docking of the two halves of LRRK2^{RCKW} into a cryo-EM map of a LRRK2^{RCKW} dimer solved in the presence of MLi-2. The dimer map is the same one shown in Fig. 3 and Extended Data Figs. 10 and 11. **d**, The model obtained in (c) was docked into cryo-EM maps of either WD40- or COR-mediated dimers obtained in the presence of MLi-2. **e**, Molecular models resulting from the docking in (d). **f**, Aligning, in alternating order, copies of the dimer models generated in (d, e) results in a right-handed filament with dimensions compatible with those of a microtubule, and its RoC domains pointing inwards (see Fig. 3g–i for more details). **g**, Docking of the two halves of LRRK2^{RCKW} into a cryo-EM map of a LRRK2^{RCKW} monomer solved in the absence of inhibitor ("Apo"). The map is the one shown in Fig. 1h and Extended Data Fig. 6. **h**, Three-way comparison of LRRK2^{RCKW} (with domain colours) and the models resulting from the dockings into the MLi-2 WD40-mediated dimer map (c) (dark blue) and "Apo" monomer map (g) (light blue). The three structures were aligned using the C-lobes of their kinases and the WD40 domain. The superposition illustrates that the docking into the "Apo" map results in a structure very similar to that obtained from the trimer (Fig. 1) and that the presence of MLi-2 leads to a closing of the kinase. **i**, Molecular model of the microtubule-associated LRRK2^{RCKW} filament obtained by docking a fragment of a microtubule structure (PDB: 6O2S) into the corresponding density in the sub-tomogram average (Fig. 2a). **j**, Same view as in (i) with the models shown as surface representations colored by their Coulomb potential. **k, l**, "Peeling off" of the structure shown in (j), with the LRRK2^{RCKW} filament seen from the perspective of the microtubule surface (k) and the microtubule surface seen from the perspective of the LRRK2^{RCKW} filament (l). Note: the acidic C-terminal tubulin tails are not ordered in the microtubule structure and thus are not included in the surface charge distributions. The Coulomb potential coloring scale is shown on the right.

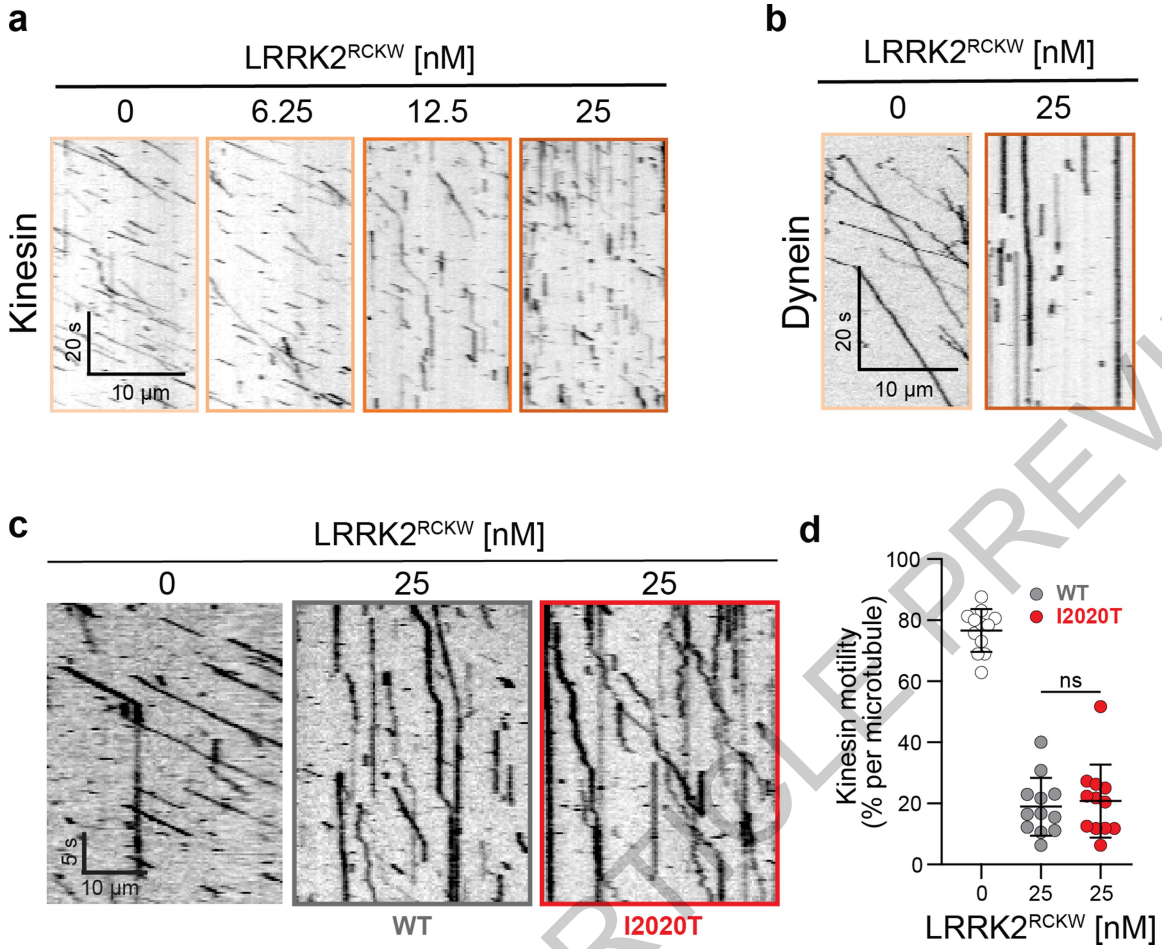

Extended Data Fig. 8 | Inhibition of motor motility by wild-type and I2020T LRRK2^{RCKW}. **a**, Example kymographs showing that increasing concentrations of LRRK2^{RCKW} reduce kinesin runs. **b**, Example kymographs showing that 25 nM LRRK2^{RCKW} reduces dynein runs. **c**, Representative kymographs of kinesin motility in the presence or absence of WT and I2020T LRRK2^{RCKW}. **d**, The percentage of motile kinesin events per microtubule in the absence of LRRK2 or in the presence of 25 nM WT or I2020T LRRK2^{RCKW}. Data are mean ± s.d. ($n = 12$ microtubules per condition quantified from two independent experiments). There is a significant difference between 0 nM and both 25 nM RCKW conditions ($P < 0.0001$), but no significant (ns) difference between the inhibitory effects of WT LRRK2^{RCKW} versus I2020T LRRK2^{RCKW} as calculated using the Kruskal–Wallis test with Dunn's posthoc for multiple comparisons (compared to no LRRK2^{RCKW}).

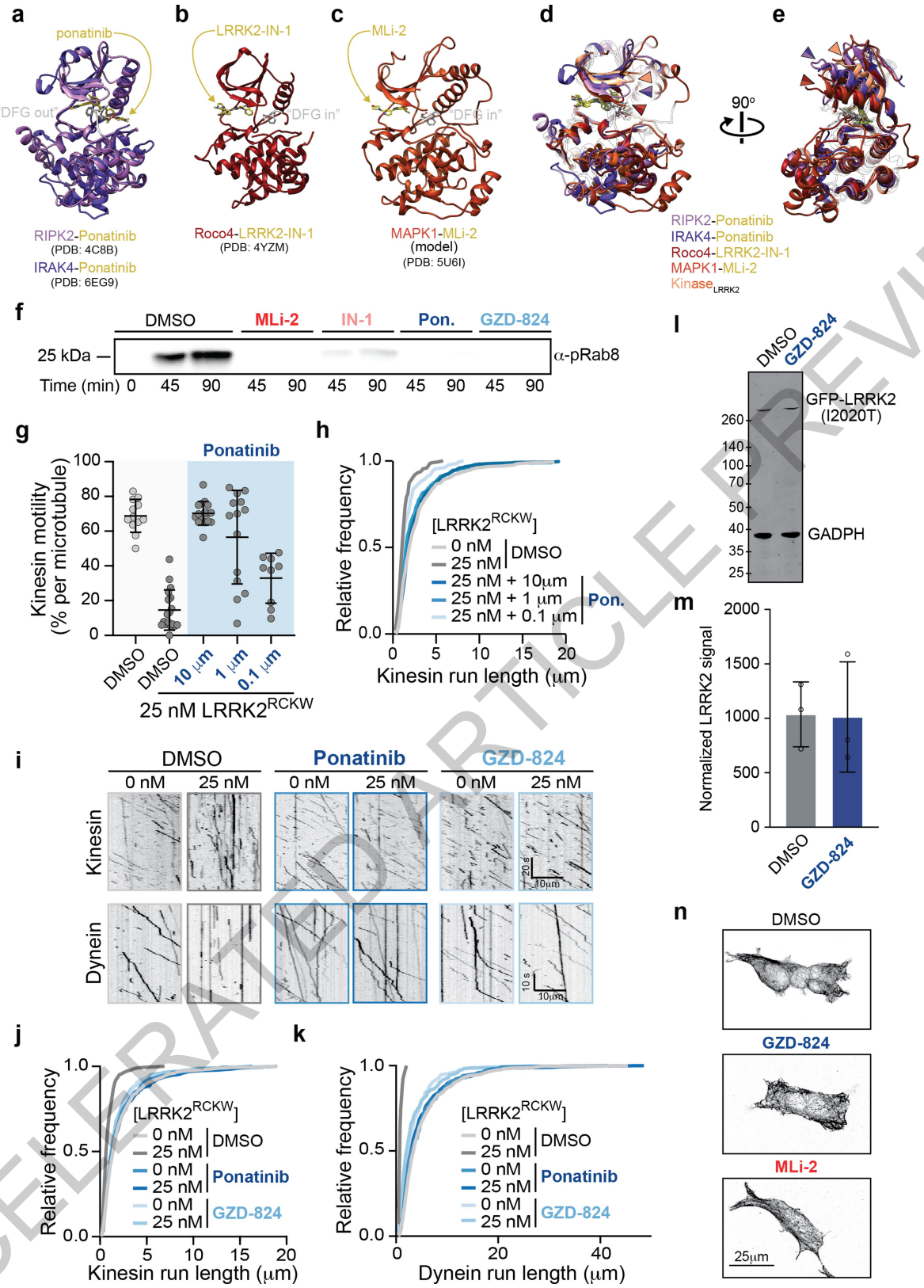

Extended Data Fig. 9 | See next page for caption.

Extended Data Fig. 9 | Type II kinase inhibitors rescue kinesin and dynein motility. a-e, Ponatinib is a Type II, "DFG out" inhibitor. **a**, Superposition of the structures of Ponatinib-bound RIPK2 (PDB: 4C8B)[32] and IRAK4 (PDB: 6EG9). Ponatinib is shown in yellow, and the DYG motif residues are shown in white. **b**, **c** For comparison, the structures of (a) Roco4 bound to LRRK2-IN-1 (PDB: 4YZM)[35], a LRRK2-specific Type I, "DFG in" inhibitor, and (b) a model of Mitogen-activated kinase 1 (MAPK1) bound to MLi-2 (PDB: 5U6I)[22], another LRRK2-specific Type I, "DFG in" inhibitor are shown. The inhibitor and DFG residues are colored as in (a). **d**, The structures in (a-c), as well as the kinase from $LRRK2^{RCKW}$ are shown superimposed. The colour arrowheads point to the N-lobe's β-sheet to highlight the difference in conformation between kinases bound to the two different types of inhibitors. Note that $LRRK2^{RCKW}$'s kinase is even more open than the two Ponatinib-bound kinases. **e**, Rotated view of (d), now highlighting the position of the N-lobe's αC helix. An additional alpha helix in the N-lobe of MAPK1 was removed from this view for clarity. **f**, The kinase inhibitors MLi-2 (1 μM), LRRK2-IN-1 (1 μM), Ponatinib (10 μM) and GZD-824 (10 μM) all inhibit $LRRK2^{RCKW}$'s kinase activity in vitro compared to a DMSO control. A western blot using a phospho-specific antibody to Rab8a at the indicated time points is shown. **g**, A dose response curve showing the percentage of motile kinesin events per microtubule as a function of Ponatinib concentration with $LRRK2^{RCKW}$ (25 nM) or without $LRRK2^{RCKW}$. Data are mean ± s.d. (from left to right: n = 12, 18, 16, 14, and 9 microtubules quantified from one experiment). ****P < 0.0001 (Kruskal–Wallis test with Dunn's posthoc for multiple comparisons, compared to DMSO without $LRRK2^{RCKW}$). **h**, Dose response curve of run lengths from data in (g) represented as a cumulative frequency distribution. From top to bottom: n = 654, 173, 584, 293, and 129 motile kinesin events. Mean decay constants (tau) ± confidence interval (CI) are (from top to bottom) 2.736 ± 0.113, 1.291 ± 0.181, 2.542 ± 0.124, 2.285 ± 0.134, and 1.653 ± 0.17. **i**, Representative kymographs of kinesin and dynein with DMSO or Type II inhibitors with or without $LRRK2^{RCKW}$. **j**, The Type II kinase inhibitors Ponatinib and GZD-824 rescue kinesin run length, represented as a cumulative frequency distribution of run lengths with $LRRK2^{RCKW}$ (25 nM) or without $LRRK2^{RCKW}$. From top to bottom: n = 893, 355, 507, 499, 524, and 529 runs from two independent experiments. Mean decay constants (tau) ± 95% CI are (from top to bottom) 2.070 ± 0.058, 0.8466 ± 0.091, 1.938 ± 0.065, 2.075 ± 0.07, 1.898 ± , 0.065, and 1.718 ± 0.064. Data were resampled with bootstrapping analysis and statistical significance was established using a one-way ANOVA with Dunnett's test for multiple comparisons. DMSO run lengths were significantly different (P < 0.0001) between conditions (0 vs. 25 nM RCKW). Ponatinib (0 vs. 25 nM RCKW) and GZD-824 (0 vs. 25 nM LRRK2) were not significant. **k**, Same as in (j) but with dynein. From top to bottom: n = 659, 28, 289, 306, 254, and 339 runs from two independent experiments. Mean decay constants (tau) ± 95% confidence intervals; microns are 4.980 ± 0.147, 0.846 ± 0.415, 4.686 ± 0.142, 4.445 ± 0.172, 3.156 ± 0.09, 3.432 ± 0.188 (from top to bottom). Statistical significance as in (j) and run lengths were significantly different (P < 0.0001) between DMSO conditions (0 vs. 25 nM RCKW), and not significant for Ponatinib or GZD0824 conditions. The DMSO conditions are reproduced from Fig. 4f for comparison. **l**, Expression levels of GFP-LRRK2 (I2020T) in 293T cells treated with either DMSO or GZD-824 (5 μM). An Immunoblot with anti-GFP (LRRK2) and anti-GADPH (loading control), which is a representative image from three replicates, is shown. **m**, Quantification of GFP-LRRK2 (I2020T) expression levels from western blots similar to (l). Data are mean ± s.d. (n = 3 per condition). GZD-824 is not significantly different from the DMSO-treated control (Mann–Whitney test). **n**, 293T cells immunostained for tubulin showing that the microtubule architecture is not affected by GZD-824 or MLi-2 compared to DMSO treatment. See Supplementary Table 1 for all source data and replicate information.

Extended Data Table 1 | Cryo-EM data collection and model refinement statistics.

	Trimer Dataset	Monomer (Apo) Dataset	Dimers (Apo) Dataset	Dimers (MLi-2) Dataset
Data Collection				
Number of grids used	1	10	3	2
Microscope	Titan Krios	Talos Arctica	Talos Arctica	Talos Arctica
Camera	Gatan K2	Gatan K2	Gatan K2	Gatan K2
Camera Mode (Counting/Super-Res.)	C	C/SR	C/SR	C
Voltage (kV)	300	200	200	200
Magnification	130,000	36,000	36,000	36,000
Pixel size (Å/pixel)	1.07	1.16/0.58	1.16/0.58	1.16
Dose rate (e^-/Å^2 second)	6.65	4.2-10	4.6-7.8	5.5
Exposure time (s)	8	6-12	7-11	9-10
Total dose (e^-/Å^2)	53.2	50.4-60	50.6-54.6	49.5-55
Number of frames	40	30-60	35-55	45-50
Defocus range (μm)	1-1.8	1-2	1-2	1-2
Micrographs collected (no.)	3,824	11,354	5,303	4,139
Initial particle number	836,956	1,184,330	431,387	706,807
Final particle number	70,954*/ 105,787#	15,999	63,435[a]/ 21,497[b]	72,249[a]/ 36,727[b]
Final Resolution (0.143 FSC threshold) (Å)	3.5*/3.8#	8.1	13.4[a]/9.5[b]	10.2[a]/9.0[b]

LRRK2^{RCKW} Models	**(without GDP-Mg^{2+})**		**(with GDP-Mg^{2+})**	
	Monomer w/interfaces PDB: 6VP8 EMD-21250	**Top 10 Monomers**** PDB: 6VP7 EMD-21250	**Monomer w/interfaces** PDB: 6VP6 EMD-21250	**Top 10 Monomers**** PDB: 6VNO EMD-21250
Model Refinement				
Map-to-model resolution (0.143 FSC threshold) (Å)	3.98	3.98	3.98	3.98
Map B-factor (Å^2)	-136	-136	-136	-136
Model Composition				
Non-hydrogen atoms	13,161	8,534	13,161	8,534
Protein Residues	1,668	1,084	1,668	1,084
Ligands	0	0	1	1
B-factors (Å^2)				
Protein	42.75	49.76	45.49	50.4
Ligand	-	-	193.78	193.78
R.M.S. Deviations				
Bond length (Å)	0.013	0.013	0.090	0.112
Bond angle (°)	1.374	1.384	2.238	2.596
Validation				
Molprobity score	1.37	1.48	1.42	1.51
Clash score	1.69	2.35	2.03	2.61
Poor rotamers (%)	0.00	0.00	0.00	0.00
Ramachandran				
Favored (%)	92.90	92.58	93.02	92.57
Allowed (%)	5.99	6.36	5.99	6.32
Disfavored (%)	1.11	1.06	0.99	1.11

The model refinement statistics are reported for four different types of models, two including GDP-Mg^{2+} in the RoC domain and two excluding it. In each case, we report statistics for two types of model: "Monomer w/interfaces" consists of a LRRK2^{RCKW} monomer plus fragments from the neighbouring monomers in the C3 trimer that were used during model building and refinement; "Top 10 Monomers" are the top-10 results from Rosetta Relax with the neighbouring fragments removed after processing in Rosetta. PDB accession numbers for the models and the EMD code of the maps used for model-building and refinement are indicated. EMD-21250 contains both the C3 map of the LRRK2^{RCKW} trimer used to build the COR-B, kinase and WD40 domains and the signal-subtracted monomer used to build the RoC and COR-A domains. The final models reported here were refined into the signal-subtracted monomer map. (See Methods for details.) * C3 reconstruction. # signal-subtracted monomer. [a] WD40-mediated dimer. [b] COR-mediated dimer. ** Numbers represent the average of the values for all 10 models.

nature research

Corresponding author(s): Samara L Reck-Peterson and Andres E Leschziner

Last updated by author(s): Aug 6, 2020

Reporting Summary

Nature Research wishes to improve the reproducibility of the work that we publish. This form provides structure for consistency and transparency in reporting. For further information on Nature Research policies, see Authors & Referees and the Editorial Policy Checklist.

Statistics

For all statistical analyses, confirm that the following items are present in the figure legend, table legend, main text, or Methods section.

n/a	Confirmed
☐	☒ The exact sample size (*n*) for each experimental group/condition, given as a discrete number and unit of measurement
☐	☒ A statement on whether measurements were taken from distinct samples or whether the same sample was measured repeatedly
☐	☒ The statistical test(s) used AND whether they are one- or two-sided *Only common tests should be described solely by name; describe more complex techniques in the Methods section.*
☒	☐ A description of all covariates tested
☐	☒ A description of any assumptions or corrections, such as tests of normality and adjustment for multiple comparisons
☐	☒ A full description of the statistical parameters including central tendency (e.g. means) or other basic estimates (e.g. regression coefficient) AND variation (e.g. standard deviation) or associated estimates of uncertainty (e.g. confidence intervals)
☐	☒ For null hypothesis testing, the test statistic (e.g. *F*, *t*, *r*) with confidence intervals, effect sizes, degrees of freedom and *P* value noted *Give P values as exact values whenever suitable.*
☒	☐ For Bayesian analysis, information on the choice of priors and Markov chain Monte Carlo settings
☒	☐ For hierarchical and complex designs, identification of the appropriate level for tests and full reporting of outcomes
☒	☐ Estimates of effect sizes (e.g. Cohen's *d*, Pearson's *r*), indicating how they were calculated

Our web collection on statistics for biologists contains articles on many of the points above.

Software and code

Policy information about availability of computer code

Data collection	For electron microscopy experiments, data was collected with Leginon. All the electron microscopy data collection software sources are referenced in the methods section. For light microscopy experiments, data was collected with Nikon Elements Software (commercially available). For Western blot, data was collected using Image Studio v5.2 (Li-COR).
Data analysis	For electron microscopy experiments, data was processed with Appion, GCTTF, MotionCor2, FindEM, Cryolo, Relion3, and Cryosparc2. All the electron microscopy data processing software sources are referenced in the methods section. For light microscopy experiments, data was analyzed with ImageJ and used to make image z-maximum projections and kymographs. Graphpad Prism8 were used for all statistical analysis of light microscopy data. For Western blots, data was quantified using EmpiriaStudio software (Li-COR).

For manuscripts utilizing custom algorithms or software that are central to the research but not yet described in published literature, software must be made available to editors/reviewers. We strongly encourage code deposition in a community repository (e.g. GitHub). See the Nature Research guidelines for submitting code & software for further information.

Data

Policy information about availability of data

All manuscripts must include a data availability statement. This statement should provide the following information, where applicable:

- Accession codes, unique identifiers, or web links for publicly available datasets
- A list of figures that have associated raw data
- A description of any restrictions on data availability

For electron microscopy experiments, maps and coordinates are deposited on the PDB and EMDB. No image sets or particle stacks will be made available. All the raw data that went into the biochemical and cell biological analyses for Figures 4 and 5 (and associated Extended Data Figures) were deposited in a spreadsheet with the manuscript.

Field-specific reporting

Please select the one below that is the best fit for your research. If you are not sure, read the appropriate sections before making your selection.

☒ Life sciences ☐ Behavioural & social sciences ☐ Ecological, evolutionary & environmental sciences

For a reference copy of the document with all sections, see nature.com/documents/nr-reporting-summary-flat.pdf

Life sciences study design

All studies must disclose on these points even when the disclosure is negative.

Sample size	For all experiments, we determined the sample size by following conventions in the field.
Data exclusions	For single molecule kinesin experiments, clear bright aggregates (less than 5% of runs) were excluded from the analysis, as these runs display longer run lengths than typical single-molecule kinesin runs (Brouhard, 2010, Methods Cell Biol). No conclusions change with the addition or exclusion of these aggegrates, and we would be happy to provide the data without exclusion of aggregates if deemed necessary.
Replication	All single molecule experiments in Figure 4 and 5 (including dynein and kinesin data with or without drugs) were performed with at least two, but up to four technical replicates on different days (except EDF10g,h that was only performed with one technical replicate). Major findings with kinesin and dynein single molecule data have been confirmed by two different protein preps. All cellular data from Figure 5 was quantified from at least four, but up to ten technical replicates (defined in the Methods as at least 20 cells per coverslip) and independent experiments were performed on multiple days as outlined in the Methods section.
Randomization	This is not relevant. We have no data involving organisms or subjects that would require randomization.
Blinding	For the cell biology data in Fig 5c-f, experimenter was blinded to conditions for both the imaging acquisition and analysis of LRRK2 filaments.

Reporting for specific materials, systems and methods

We require information from authors about some types of materials, experimental systems and methods used in many studies. Here, indicate whether each material, system or method listed is relevant to your study. If you are not sure if a list item applies to your research, read the appropriate section before selecting a response.

Materials & experimental systems

n/a	Involved in the study
☐	☒ Antibodies
☐	☒ Eukaryotic cell lines
☒	☐ Palaeontology
☒	☐ Animals and other organisms
☒	☐ Human research participants
☒	☐ Clinical data

Methods

n/a	Involved in the study
☒	☐ ChIP-seq
☒	☐ Flow cytometry
☒	☐ MRI-based neuroimaging

Antibodies

Antibodies used	mouse anti-GFP (Santa Cruz, clone: B-2, Cat: sc-9996, Lot:); chicken anti-GFP (AvesLabs, Cat: GFP-1010, Lot: GFP879484); rabbit anti-alpha-tubulin (ProteinTech, Cat: 11224-1-AP); mouse anti-GAPDH (ProteinTech, Cat: 60004-1-Ig)
Validation	All antibodies used are well-validated and highly-specific commercially available antibodies. For LiCOR quantification, linear

Eukaryotic cell lines

Policy information about cell lines

Cell line source(s)	HEK293T used were from ATCC (CRL-3216)
Authentication	ATCC authenticated
Mycoplasma contamination	Every new cell line we receive is tested for mycoplasma before expanding and freezing. After thawing, each cell line is tested again. Once every three months, our lab tests all growing cells for mycoplasma as well. The cells we used in our experiments were last test on 10/16/19 and did not contain contamination.
Commonly misidentified lines (See ICLAC register)	None